AGU PUBLICATIONS

JGR

Journal of Geophysical Research: Oceans

RESEARCH ARTICLE

10.1002/2016JC012444

Flow paths and variability of the North Atlantic Current: A comparison of observations and a high-resolution model

Tilia Breckenfelder[1,2], Monika Rhein[1,2], Achim Roessler[1,2], Claus W. Böning[3], Arne Biastoch[3], Erik Behrens[4], and Christian Mertens[1,2]

[1]University of Bremen, Institute of Environmental Physics, Bremen, Germany, [2]MARUM—Center for Marine Environmental Sciences, Bremen, Germany, [3]GEOMAR Helmholtz Centre for Ocean Research Kiel, Kiel, Germany, [4]National Institute for Water and Atmospheric Research, Wellington, New Zealand

Key Points:
- Detailed comparison between high-resolution VIKING20 model and observations reveal realistic flow fields in the subpolar North Atlantic
- North Atlantic Current transports in model and observations are comparable within the uncertainties
- The NAO influences the transport and flow field of the North Atlantic Current; higher transports occur during positive phases

Correspondence to:
T. Breckenfelder,
t.breckenfelder@uni-bremen.de

Citation:
Breckenfelder, T., M. Rhein, A. Roessler, C. W. Böning, A. Biastoch, E. Behrens, and C. Mertens (2017), Flow paths and variability of the North Atlantic Current: A comparison of observations and a high-resolution model, *J. Geophys. Res. Oceans*, *122*, doi:10.1002/2016JC012444.

Received 7 OCT 2016
Accepted 2 MAR 2017
Accepted article online 7 MAR 2017

Abstract The North Atlantic Current (NAC) is subject to variability on multiannual to decadal time scales, influencing the transport of volume, heat, and freshwater from the subtropical to the eastern subpolar North Atlantic (NA). Current observational time series are either too short or too episodic to study the processes involved. Here we compare the observed continuous NAC transport time series at the western flank of the Mid-Atlantic Ridge (MAR) and repeat hydrographic measurements at the OVIDE line in the eastern Atlantic with the NAC transport and circulation in the high-resolution (1/20°) ocean model configuration VIKING20 (1960–2008). The modeled baroclinic NAC transport relative to 3400 m (24.5 ± 7.1 Sv) at the MAR is only slightly lower than the observed baroclinic mean of 27.4 ± 4.7 Sv from 1993 to 2008, and extends further north by about 0.5°. In the eastern Atlantic, the western NAC (WNAC) carries the bulk of the transport in the model, while transport estimates based on hydrographic measurements from five repeated sections point to a preference for the eastern NAC (ENAC). The model is able to simulate the main features of the subpolar NA, providing confidence to use the model output to analyze the influence of the North Atlantic Oscillation (NAO). Model based velocity composites reveal an enhanced NAC transport across the MAR of up to 6.7 Sv during positive NAO phases. Most of that signal (5.4 Sv) is added to the ENAC transport, while the transport of the WNAC was independent of the NAO.

1. Introduction

The subpolar North Atlantic is characterized by considerable variability in water mass transformation and transports on intraseasonal to multidecadal time scales, with some of the variability connected to atmospheric modes like the North Atlantic Oscillation (NAO) [e.g., *Curry and McCartney*, 2001; *Häkkinen and Rhines*, 2004; *Brauch and Gerdes*, 2005; *Kieke et al*., 2007; *Hauser et al*., 2015; *Delworth and Zeng*, 2016]. The transport of warm and salty water in the upper ocean from the subtropics into the Newfoundland basin (Figure 1) is carried by the northward extension of the Gulf Stream and dubbed North Atlantic Current (NAC). Part of the NAC recirculates to the south in the interior of the Newfoundland basin [e.g., *Mertens et al*., 2014]. A fraction of the NAC transport continues north to the southern Labrador Sea where it retroflects to the east forming the Northwest Corner (NWC) [*Rossby*, 1996]. Ultimately the NAC crosses the Mid-Atlantic Ridge (MAR) into the eastern basin, forming the southern rim of the cyclonic subpolar gyre (SPG), the main circulation feature in this region. In the Newfoundland Basin and at the MAR, the velocity field in the NAC is deep reaching [*Rhein et al*., 2011; *Mertens et al*., 2014; *Roessler et al*., 2015] and is influenced by the presence of fracture zones (Figure 1), mainly the Charlie Gibbs Fracture Zone (CGFZ), the Faraday Fracture Zone (FFZ), and the Maxwell Fracture Zone (MFZ) [e.g., *Bower and von Appen*, 2008].

The buoyancy loss of the NAC by the cooling along its northward pathway contributes to the formation of Labrador Sea Water in the Labrador Sea [*Talley and McCartney*, 1982], and connects the warm upper branch and the cold lower branch of the Atlantic Meridional Overturning Circulation (AMOC). Based on projections from climate models, it is expected that global warming will cause significant changes in the circulation as well as the temperature and salinity properties of water masses formed there. This in turn will lead to changes in meridional heat and freshwater fluxes, which could have consequences for the future climate and sea level in western Europe [*Intergovernmental Panel on Climate Change* (*IPCC*), 2013].

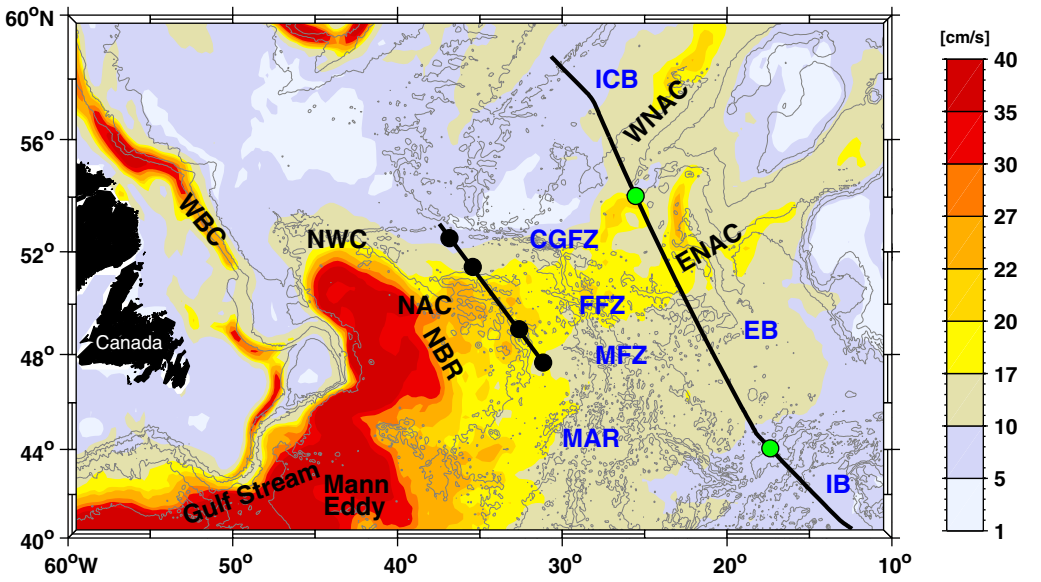

Figure 1. Map of the subpolar North Atlantic with the mean sea surface speed from gridded geostrophic velocity provided by AVISO and bottom topography from ETOPO2 database [*U.S. Department of Commerce*, 2001], indicated by gray lines with a depth interval of 1000 m between 5000 m depth and the surface. Abbreviations: North Atlantic Current (NAC), Western Boundary Current (WBC), Northwest Corner (NWC), western NAC (WNAC), eastern NAC (ENAC), Newfoundland Basin Recirculation (NBR), Charlie-Gibbs Fracture Zone (CGFZ), Faraday Fracture Zone (FFZ), Maxwell Fracture Zone (MFZ), Mid-Atlantic Ridge (MAR), Iceland Basin (ICB), European Basin (EB), and Iberian Basin (IB). The positions of the PIES at the MAR are marked by the black dots. The PIES divide the array in a northern, a central and a southern segment. North of the PIES the model extended section is shown (by the thick inclined black line across the PIES positions), needed to take into account the more northward pathways of the NAC in the model. The black line from 40°N to 58°N is the OVIDE line. The green dots indicate the geographical separation of the OVIDE line in Iceland Basin, European Basin and Iberian Basin following *Mercier et al.* [2015].

Although the importance of the NAC as part of the climate relevant meridional overturning of the Atlantic is widely known, continuous measurements of the NAC transport and its variability away from the western boundary are rare and too short to study decadal fluctuations. In *Rhein et al.* [2011], the first continuous 2 year long (2006–2008) NAC transport time series at the MAR calculated from an array of bottom mounted inverted echo sounders equipped with a pressure sensor (PIES) instruments was published. *Roessler et al.* [2015] used the correlation between the PIES derived baroclinic transport time series (2006–2010) at the MAR and the sea level anomalies from altimetry to extend the transport time series to the time period of altimeter data from 1992 to 2013. They argue that the annually averaged time series is close to the absolute transports, although they assume a zero transport at a reference level of 3400 dbar. The 21 year mean was 27.4 Sv (with a standard deviation of 4.7 Sv), consisting of about 60% water with subtropical (16.0 Sv, densities < 27.68 kg m^{-3}), and 40% with subpolar origin. No long-term trend was found, but substantial variability on time scales of 120 days (meanders, eddies) and 4–9 years, with the latter partly explained by the North Atlantic Oscillation (NAO) index.

Lherminier et al. [2010], *Mercier et al.* [2015], *García-Ibáñez et al.* [2015], and *Daniault et al.* [2016] analyzed repeat hydrographic and velocity (from vessel mounted Acoustic Doppler Current Profiler (ADCP)) sections from Greenland to Portugal in the OVIDE (Observatoire de la Variabilité Interannuelle à Décennale) program. These hydrographic measurements were carried out between 1997 and 2012. The authors calculated the full depth absolute circulation using an inverse model constrained by the ADCP data and by an overall mass balance. They found large transport variability over the whole water column. The mean NAC transport above the $\sigma_1 = 32.1$ kg m^{-3} isopycnal was 16 Sv, and equally split between the eastern (ENAC) and the western (WNAC) branch of the NAC [*Lherminier et al.*, 2010]. These numbers are similar to the mean NAC transport of 15.5 Sv (densities < 27.55 kg m^{-3}), that *Sarafanov et al.* [2012] calculated from hydrographic repeated sections at 59.5°N, measured annually between 2002 and 2008. Both estimates from repeat hydrography are comparable to the mean continuously measured NAC transport (1992–2013) of subtropical water crossing the MAR [*Roessler et al.*, 2015].

In this study, we try to obtain new insights about seasonal to decadal variability and pathways of the NAC, by comparing observational against model data of a high-resolution model configuration (VIKING20), at the

PIES array along the MAR and in the eastern Atlantic across the OVIDE section. Encouraging for this study was the similarities between observational data and the VIKING20 model at 47°N in the western Newfoundland basin [*Mertens et al*., 2014]. The main vertical and horizontal circulation features, the strength of the NAC inflow into the Newfoundland basin, and the NAC recirculation (NBR) were well simulated by the VIKING20 model, so that *Mertens et al*. [2014] used the model to discuss the relation between the variability found in the deep western boundary current (DWBC), the NAC, and the NAC recirculation. Here we extend the analysis of observations and model farther to the east to study the mean transport and the variability on interannual to decadal time scales, the density distributions, and the locations of NAC branches over time. The focus of this study lies on a detailed comparison between the model output and observations. Furthermore, encouraged by the agreement between these two data sources we use the model to discuss the relation between the strength and the pathways of the NAC and the state of the atmospheric circulation expressed in the NAO index.

The paper is organized as follows: after the data and methods section (section 2), we compare the model output with observations in section 3. We start with a general comparison of the circulation in the North Atlantic (NA) before focusing on the vertical hydrographic and velocity distributions at the MAR (section 3). The mean transports at several positions in the NA between model and observations are compared, with the focus on the NAC transports across the MAR and in the eastern basin of the NA across the OVIDE line. Based on the confidence, we gain from the comparison between model and observations we concentrate in the discussion and conclusion section (section 4) on the pathways of the NAC and the influence of the NAO on the NA and the transport of the NAC.

2. Data and Methods

2.1. VIKING20 Model Configuration

The VIKING20 model configuration is based on the NEMO ocean [*Madec*, 2008] and LIM2 sea ice [*Fichefet and Maqueda*, 1997] model, developed in the DRAKKAR framework [*DRAKKAR*, 2007]. This configuration uses a local grid refinement technique (AGRIF) [*Debreu et al*., 2008], which allows a high-resolution nest to be coupled into a coarser grid via a two-way nesting scheme [*Behrens*, 2013; *Böning et al*., 2016]. In the case of the VIKING20 configuration, the coarser grid is a global tri-polar ORCA025 grid with a nominal 1/4° horizontal resolution [*Barnier et al*., 2006]. Embedded in this grid is a high-resolution nest covering the North Atlantic between 32°N and 80°N, with grid sizes of 1/20°. The vertical grid of this configuration uses 46 vertical levels, with a 6 m thick surface layer, and increasing with depths to up to layer thickness of 250 m at around 1000 m. A partial cell approach is implemented to improve the near topographically steered circulation [*Barnier et al*., 2006]. In this study, we use 5 day averaged model fields for the period 1960–2008 from this model hindcast, which was forced with interannually varying atmospheric conditions based on CORE.v2 reanalysis product [*Large and Yeager*, 2009]. The simulation was started from rest with initial condition based on Levitus [*Levitus*, 1998] and followed by a 30 year long spin-up simulation before the reference hindcast has been started in 1948. The model was already compared to observations in the subpolar North Atlantic in several studies [*Fischer et al*., 2014; *Mertens et al*., 2014; *Böning et al*., 2016]. In *Fischer et al*. [2014], the variability of the DWBC transport from Denmark Strait to the tail of the Grand Banks was investigated using seven observational sections in comparison to the VIKING20 model in order to relate the local observations to the large scale perspective. They reported that the DWBC in the model has its maximum variance at intra seasonal periods and the best agreement between the modeled and observed spectra is found for the Flemish Cap section at 47°N.

Along this 47°N section between Flemish Cap and 36°W *Mertens et al*. [2014] studied the strength of the NAC inflow into the Newfoundland basin, the NAC recirculation and the DWBC from seven cruises and moored data in comparison to the VIKING20 model.

The meltwater from the West Greenland shelf was found to be influencing the surface salinity in the central Labrador Sea in the VIKING20 model [*Böning et al*., 2016]. The study also showed that decadal freshwater content anomalies in the subpolar NA, which have been observed by *Curry and Mauritzen* [2005] and *Boyer et al*. [2007], can be successfully simulated.

The model was initialized with the World Ocean Atlas (WOA) 1998 [*Levitus*, 1998] salinity climatology (Figure 2a), derived from data for the years 1900–1997. This climatology and the mean VIKING20 salinity

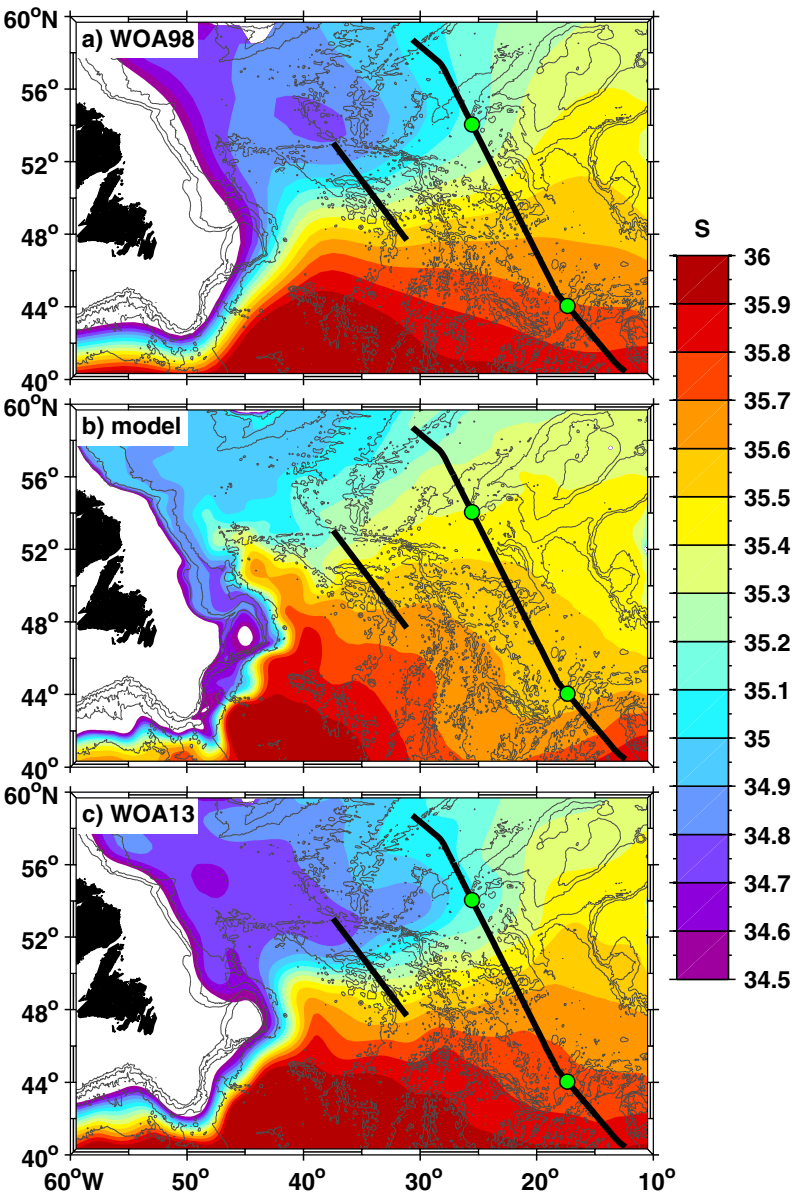

Figure 2. Salinity distribution in 100 m depth from (a) WOA 1998 climatology, (b) the VIKING20 model mean from 1960 to 2008, and (c) the WOA 2013 climatology.

distribution (1960–2008) in 100 m depths are comparable. However, owing to the resolution the salinity distribution in the model (0.05° resolution) is more detailed compared to the coarse climatology (1° resolution). Observed salinities in the central and northern Labrador Sea (Figure 2a) are fresher than found in the model (Figure 2b). This is even enhanced when compared to the WOA 2013 [*Zweng et al*., 2013] climatology (Figure 2c), which is the average of six "decadal" climatologies for the following time periods: 1955–1964, 1965–1974, 1975–1984, 1985–1994, 1995–2004, and 2005–2012 [*Zweng et al*., 2013]. The NWC in the model evolved nicely from the WOA 1998 climatology NWC to a similar NWC as in the WOA 2013, which comprises the entire model time period. The northwestern extension of the NWC in the model (Figure 3a) is reflected by high salinities signatures along the western flank of the Labrador Sea, with salinities >35.4 stretching to 54°N (Figure 2b), while in the WOA 2013 data, this salinity does not reach farther than about 49°N (Figure 2c).

The salinity structures in the Eastern Atlantic also show similar patterns. In the observations south of about 49°N, the observed horizontal gradients are more or less meridional (Figures 2a and 2c), while in the model,

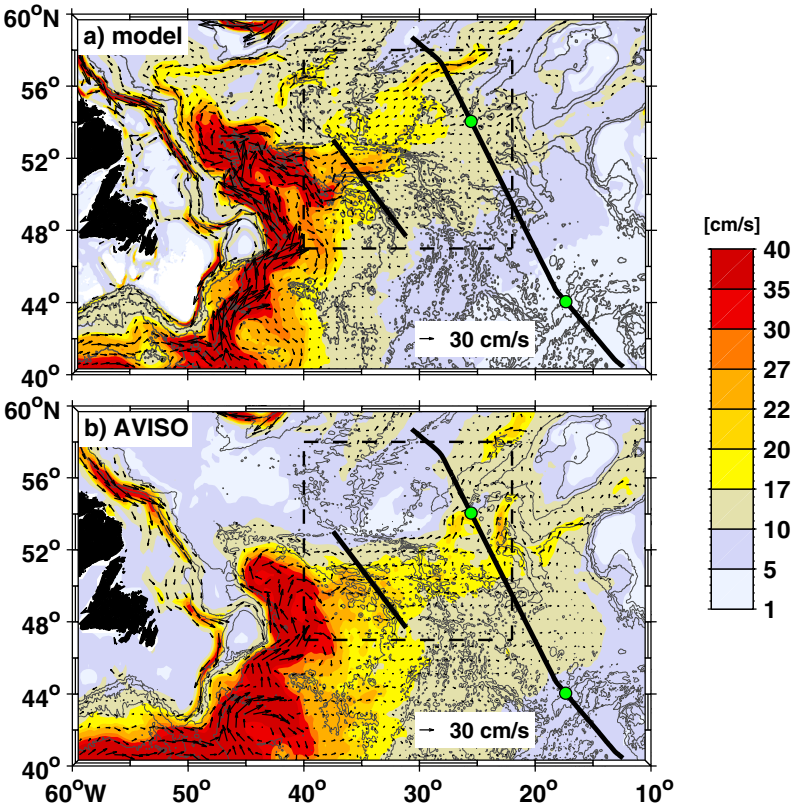

Figure 3. (a) Mean velocity at 100 m depth from the model, 1993–2008. The colors are displaying the magnitude of the velocity vectors with a resolution of 1/20°. The arrows indicate the direction of velocities >10 cm s^{-1}. The region within the dashed black lines is displayed in more detail in Figure 5. The PIES array and the OVIDE line are also shown. The bottom topography is taken from the model. (b) The same as Figure 3a but for the observed absolute surface geostrophic velocity from AVISO averaged from 1993 to 2008, resolution 1/4°. Bottom topography is taken from ETOPO2 database *U.S. Department of Commerce* [2001]. In both figures gray lines indicate the topography with a depth interval of 1000 m between 5000 m depth and the surface. For clarity the velocity vectors are displayed with a reduced resolution.

the zonal gradients dominate (Figure 2b). This leads to lower salinities in that region. North of 49°N, both, model and observations exhibit zonal gradients, but the salinities are higher in the model than in the observations. As an example the meridional salinity difference between 41°N and 57°N at 30°W in the eastern Atlantic is around 0.4 in the model and 1.0 in the observations. The higher salinities in the VIKING20 configuration is found to be related to the improvements in the NAC compared to two coarser model configurations [*Behrens*, 2013]. The salinity in the Labrador Sea rises by the increased inflow of warmer and saltier Irminger Water, which accompanied the improvement of the NAC.

2.2. Observations

2.2.1. Absolute Geostrophic Surface Velocity

The absolute geostrophic velocity used here is provided by Ssalto/Duacs and distributed by AVISO, with support from CNES (http://www.aviso.altimetry.fr/duacs/). It is computed from the maps of daily absolute dynamic topography (MADT) and has a spatial resolution of 1/4° × 1/4° on a Cartesian grid. The MADT is inferred from the sea level anomaly and the mean dynamic topography (MDT), both are referenced over a 20 year period (1993–2012). The MDT is a combination of 7 years of GRACE, 2 years of GOCE data and in situ measurements.

2.2.2. CTD/LADCP Data

To compare the water mass characteristic and the structure of the flow at the MAR, we use velocity, salinity, temperature, and pressure measurements from seven sections along the PIES array carried out between July 2008 and May 2015. The station spacing was about 20 nautical miles (nm).

The OVIDE data set comprises five repeated measurements for every second year between 2002 and 2010 and was provided by Pascale Lherminier and published in *Mercier et al.* [2015]. Along the OVIDE line about

90 hydrographic stations were taken each cruise. The station spacing was between 25 nm and less than 12 nm, depending on topographic features [*Mercier et al*., 2015].

2.3. Transport Time Series Calculation

2.3.1. Transport Time Series From Observations

2.3.1.1. PIES Array Along the MAR

The observed baroclinic transport time series from 1993 to 2008 is calculated from a combination of along-track sea surface heights (SSH) measurements (updated delayed time Sea Level Anomaly (SLA) product from AVISO) and PIES (inverted echo sounder equipped with a pressure sensor) data [*Roessler et al*., 2015]. The PIES instrument measures the round trip travel time of an acoustic signal from the bottom to the surface and the pressure at the sea floor [*Watts and Rossby*, 1977; *Chaplin and Watts*, 1984]. Argo and shipboard CTD profiles are used to calculate a transfer function to convert travel times to profiles of temperature, salinity, density, and specific volume anomaly. Based on these reconstructed time series, the geostrophic velocity distribution and transport time series are calculated relative to a reference level. *Roessler et al*. [2015] referenced the transports to the deepest common depth of the PIES (3400 dbar), which is located well below the ridge crest of the MAR. Owing to the unknown drift of the pressure sensors, only the barotropic transport fluctuations can be analyzed. Their contribution to the standard deviation of the mean 4 year transport time series exceeds the contribution from the baroclinic transport component by around one third. *Roessler et al*. [2015] used the correlation between the altimeter derived surface velocities and the baroclinic transports calculated from the PIES data to extend the 4 year transport time series to the time period of the altimeter measurements (1992–2013). The barotropic transport fluctuations were found to be not correlated with the satellite altimetry data [*Roessler et al*., 2015], therefore only the baroclinic transport component could be extended over the whole satellite time period. Following earlier studies [e.g., *Stramma et al*., 2004; *Rhein et al*., 2011], *Roessler et al*. [2015] chose the isopycnal σ_θ =27.68 kg m^{-3} to separate the warm subtropical water of the NAC above from the deep water layers below that depth and found 60% of the transport above this isopycnal. In our study, we use this same percentage to separate the observational transport at the PIES array into a subtropical and deep water component. The geographical positions of the PIES divide the section into three segments, roughly representative of the flow through Maxwell (southern segment), Faraday (central segment), and Charlie Gibbs (northern segment) fracture zones.

2.3.1.2. OVIDE Section

The absolute transports across the OVIDE line were calculated from a combination of the CTD data and shipboard Acoustic Doppler Current Profiler (sADCP) data by using an inverse model [*Lherminier et al*., 2010; *Mercier et al*., 2015]. For the transport calculations, we divide the eastern OVIDE section into the subsections Iceland (58°N–54°N), European (54°N–44°N), and Iberian (44°N–41°N) following *Mercier et al*. [2015].

The geographical positions of the two NAC branches (Figure 1) at the OVIDE line differ between model and observations. The observed WNAC branch is found between 53°30′N and 57°N, while the modeled WNAC reaches to 57°30′N. The ENAC in the observations is defined to flow between 46°N and 53°30′N, while in the model, the pathway is located between 47°30′N and 53°30′N. As stated before, the same isopycnal (σ_θ =27.68 kg m^{-3}) was used to separate the upper from the deep ocean.

2.3.2. Transport Time Series Calculation in VIKING20 Model Configuration

The observed 21 year NAC transport time series at the western flank of the MAR (PIES array) [*Roessler et al*., 2015] was calculated between the latitudes 47°40′N and 52°30′N and fully includes the flow of the NAC into the subpolar part of the eastern Atlantic. To compare the observed geostrophic transport (relative to 3400 dbar) with the model output, we calculated the transport from the modeled velocity and density fields, referenced to 3400 m. The interpolation of the model data onto the hydrographic sections is done using a bilinear interpolation. As in the observations, the water column is separated into the subtropical water mass above the σ_θ = 27.68 kg m^{-3} isopycnal and into the deep ocean below. The model section starts at the southernmost PIES position (47°40′N/31°09′W) and ends at around 53°N/37°27′W, i.e., 0.5° further north than the northernmost PIES position (52°30′N/36°51′W). This extension takes into account the more northward flow path in the model (Figure 3). An extension of the section toward the southeast did not increase the northeastward transport across the section. As in the observations, the modeled transports are separated in the three segments (northern, central, and southern segment), with an additional model segment from 52°30′N to 53°N (extended segment). The simulated and observed annual mean transports are affected by the large variability on time scales of several months to years. For a better comparison, we follow

Roessler et al. [2015] who calculated the annual means with the center around the end of January. This time interval was chosen to match the time period of the winter NAO index.

3. Results

In the following sections flow pathways, mean transports, transport time series, and vertical structure between model and observations at various locations over the NA will be compared. We start with the description of the large-scale circulation in the NA using flow field and transport estimates.

At the MAR the hydrographic properties and velocity distribution are investigated in detail, including mean, and variability. Further downstream at the OVIDE line, no continuous observed transport time series is available, yet we compare the mean transport and the hydrography.

3.1. Circulation and Mean Transport of the North Atlantic Current

The most distinct feature in the subpolar NA is the NAC, which flows from the southwest into the eastern Atlantic, via the NWC and across the MAR. The path of the NAC is clearly visible in the mean (1993–2008) near surface velocity (100 m depth) of the model (Figure 3a), and in the mean surface velocity field calculated from the altimeter observations for the same time period (Figure 3b). Along the NAC path transports from model and observations are compared on several locations and presented in Figure 4. The modeled transports (Figure 4a) are the absolute mean transports for the time period 1993–2008, the same period where observations are available. The observations at 47°N in the Newfoundland Basin (2003–2011) [*Mertens et al.*, 2014] and at the OVIDE line in the eastern Atlantic (2002, 2004, 2006, 2008, and 2010) [*Mercier*

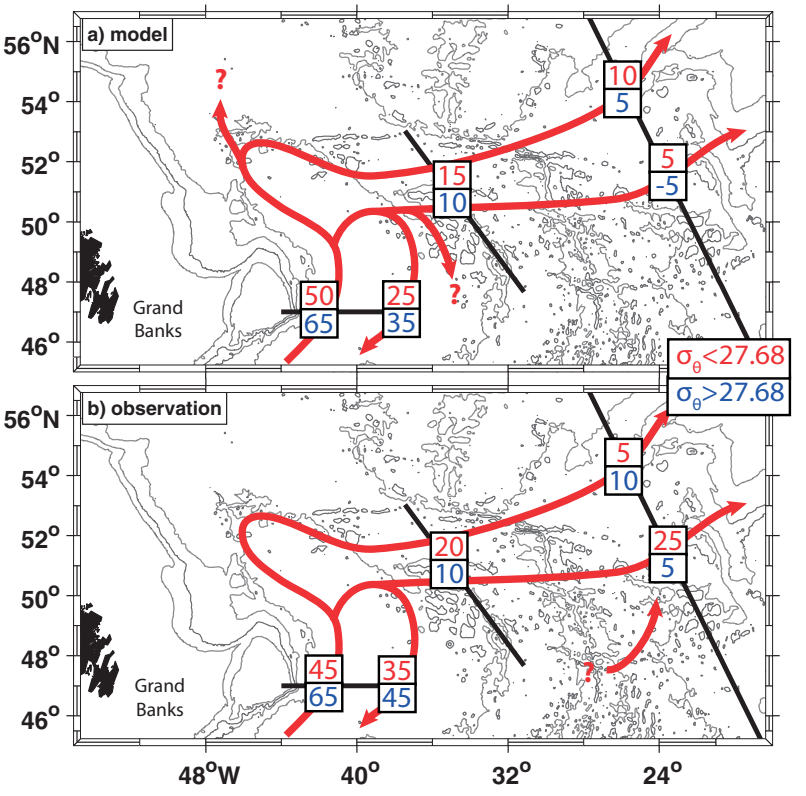

Figure 4. NAC circulation cartoon (not water masses) with (a) absolute mean transports from the model from 1993 to 2008 and (b) observed transports. The calculation of the mean transports focuses on the two observational sections, studied here and the inflow of the NAC into the NA at 47°N. The question marks indicate possible pathways influencing the means compared here. The observed NAC and NBR transports at 47°N are taken from *Mertens et al.* [2014], and are the means of six LADCP repeats taken between 2003 and 2011. The observed transport at the PIES array is the mean from 1993 to 2008, the separation into the two density ranges are done after *Roessler et al.* [2015]. Observed western and eastern NAC transports at the OVIDE line are calculated from the OVIDE data, five LADCP repeats taken between 2002 and 2010 [*Mercier et al.*, 2015]. Red numbers: NAC transport with $\sigma_\theta < 27.68$ kg m^{-3}, blue: transport of water with $\sigma_\theta > 27.68$ kg m^{-3} (after *Mertens et al.* [2014]). The transport numbers are rounded to 5 Sv.

et al., 2015] are based on several repeat hydrographic and LADCP sections, so the mean transport has large uncertainties and the numbers are rounded. A more detailed comparison with the continuous time series at the MAR follows in section 3.3, as well as a discussion about the circulation and the transport at the OVIDE line in section 3.4.

The high velocities at the continental slope off Canada and Greenland highlight the western boundary current that transports cold and freshwater to the south. The Mann Eddy (~42°N, 45°W) and the Newfoundland Basin recirculation (NBR) *Mertens et al*. [2014] centered at 47°N, 39°W are clearly visible in the model and observational velocity distributions (Figure 3).

At 47°N, the observed and simulated northward inflow of the NAC occurs close to the western boundary current and show in terms of volume transport similar strengths. These confirm the findings of *Mertens et al*. [2014], which described and compared the observed transports to a mean VIKING20 transport calculated over 47 years. They reported that the NAC carries in both cases a similar amount of transport northward and the recirculation in the Newfoundland basin seems weaker in the model.

North of 45°N, the NAC flows in close contact with the western boundary current east of Flemish Cap to about 54°N in the model (Figure 3a), and 51°N in the observations (Figure 3b). In the southern Labrador Sea, the observations depict two main pathways where the NAC retroflects to the east at about 48.5°N and 51.5°N, the latter defining the observed location of the NWC. In the model (Figure 3a), the NAC reaches further into the Labrador Sea to about 54°N before turning east. Part of the modeled mean flow seems to proceed farther north than the observations suggest. A realistic simulation of the NAC in the Newfoundland Basin has been, and continues to be, a key challenge of ocean and climate modeling. The prime model factor that influences this regional behavior is the horizontal resolution: while the common problem of coarse ocean/climate models is a southward displacement of the NAC (associated with a cold and fresh bias in the Newfoundland Basin), a typical feature of eddying models has been a northward shift of that path [*Marzocchi et al*., 2015], hinting at the importance of the mesoscale current-topography interaction along the continental slope. It is conceivable that the dynamics near the boundary are also affected by the parameterization of subgrid-scale mixing: however, to our knowledge these possible dependencies have not been examined yet (owing certainly in part to the high costs of conducting systematic model sensitivity experiments at resolutions of 1/10° or higher). One interesting hint in this regard has been given by *Smith et al*. [2000]: in their 1/10° simulation they noted a northward displacement of the NWC which partly could be remedied in a (albeit very short) sensitivity experiment with somewhat increased mixing coefficients.

The mean transport crossing the MAR is similar in the observations and in the model, about 25 Sv cross the MAR toward the eastern Atlantic, with 15 Sv of subtropical origin. The mean (1993–2008) observed flow field in the vicinity of the PIES array at the MAR (Figure 5b) shows predominant zonal velocities to the east in a broad path with the highest velocities between 48°N and 51°N, i.e., the central segment of the PIES array. Some of the NAC in the model also follows this path, although the dominant pathway there is farther north between 51°N and 53°N, exhibiting velocities that exceed 30 cm s^{-1} (Figure 5a). In the model, the NAC clearly prefers the flow through the CGFZ, while in the observations, the NAC is mainly found farther south. The preference for the CGFZ could be due to the more northern NWC in the Labrador Sea. The more northern pathway of the NAC is at least partly responsible for the higher salinities found in the eastern Atlantic north of 49°N (Figure 2b, mean modeled salinity distribution from 1960 to 2008) in the model. Furthermore, this northern NAC is fresher compared to the branch south of the CGFZ.

In the eastern Atlantic, the observations (Figures 3b and 5b) show two main NAC pathways, with the more northwestern branch (dubbed WNAC by *Lherminier et al*. [2010]) following the western flank of the Iceland basin, and the more southeastern branch (ENAC) at the Rockall Trough. In the observations, the ENAC (25 Sv) carries most of the water with $\sigma_\theta < 27.68$ kg m^{-3} (Figure 4b), while in the model, the WNAC transport is more pronounced (10 Sv) compared to the ENAC (5 Sv). This more pronounced WNAC in the model could be a consequence of the more northward NAC pathways compared to the observed flow field. The biggest discrepancy however is the observed larger ENAC transport of 25 Sv, which is larger than the modeled transports of WNAC and ENAC together. Choosing adapted boundaries for the two NAC branches instead of fixed [*Lherminier et al*., 2010] or separating the NAC flow in three branches instead of two [*Daniault et al*., 2016] modifies the observed transports of the NAC branches and makes them more comparable with the

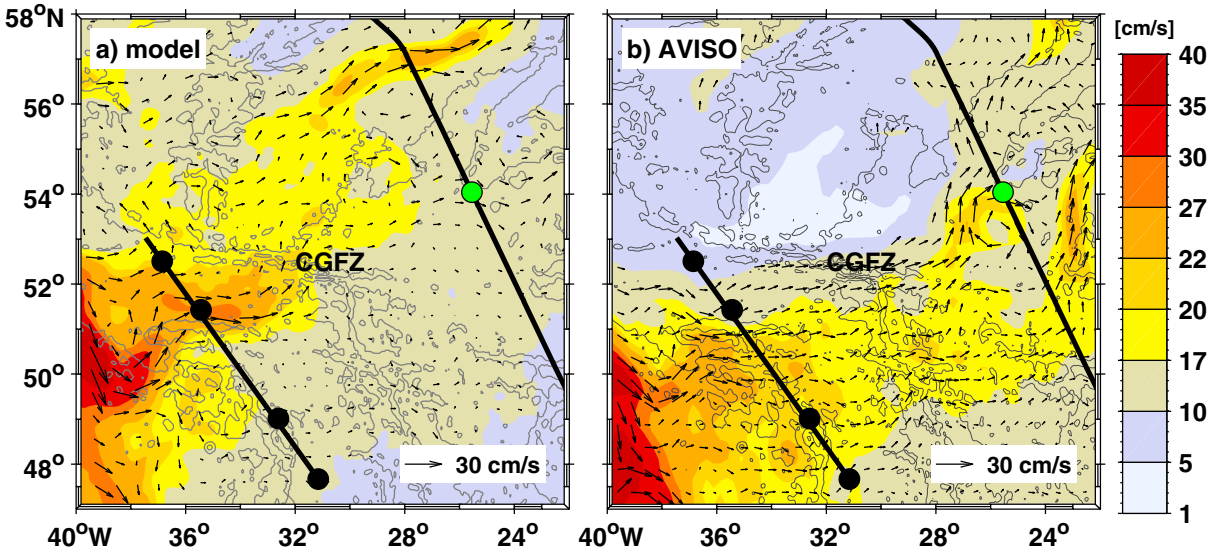

Figure 5. Velocity field as in Figure 3, but zoomed into the marked area. The black lines show the location of the PIES array at the MAR, including the model extension and the location of the OVIDE line. Black dots are the location of the PIES. The green dot indicates the geographical separation of the OVIDE line in Iceland Basin and European Basin following *Mercier et al*. [2015]. The Charlie Gibbs Fracture Zone (CGFZ) is marked. a) Mean modeled velocities at 100 m depth (1993–2008). (b) Mean geostrophic velocity at the sea surface from AVISO (1993–2008).

model results (*Lherminier et al*. [2010] with 8 Sv for each, WNAC and ENAC) or increases the discrepancies further [*Daniault et al*., 2016].

Overall, the simulated main circulation features of the NA are comparable with observations, such as the here presented altimetry data, observed transport measurements, and other observational studies using, e.g., floats at several density levels to investigate the circulation in the NA [*Lavender et al*., 2000; *Bower et al*., 2002; *Pérez-Brunius et al*., 2004]. In the model, the velocity field reveals stronger horizontal gradients compared to altimeter data, owing to the higher resolution of the model (1/20° versus 1/4°). The effect of different spatial resolution and temporal averaging on the flow field has been discussed already by *Fratantoni* [2001], who compared satellite tracked drifter trajectories and drifter derived eddy kinetic energy with values calculated from satellite altimetry.

The most remarkable differences are the shift of the NWC further into the Labrador Sea and the more northward pathways of the NAC, leading to the preference for the CGFZ and the WNAC in the model.

3.2. Vertical Hydrographic and Velocity Distributions at the MAR Array

The velocity and hydrographic distributions at the PIES array along the MAR from model and observational data are comparable in magnitude and distribution. The observations are the mean distributions of seven repeated CTD and LADCP sections between July 2008 and June 2015. The model on the other hand is the summer mean (May–July) for the last seven model years of this simulation (2002–2008). The modeled distribution is in general more saline (Figure 6a) and warmer (by about 0.5°C below 1000 m depth and 1°C above) (Figure 6c) than observed (Figures 6b and 6d). As already discussed in the horizontal distributions at 100 m depth, the VIKING20 warm and saline surface water reaches farther to the north than in the observations, but in both, model and observations, the saltiest and warmest water is found in the central and southern part of the section. The observed subtropical water north of 51°30′N is by about 0.8 fresher than in the model, so that the horizontal gradients in the observations are sharper than in the model despite the higher spatial resolution of the latter. In the deep ocean, both distributions include the Labrador Sea Water below the $\sigma_\theta = 27.68$ kg m^{-3} isopycnal, the model is warmer and more saline compared to the observations. The high salinities observed north of the subpolar front (at 52°N) at around 3000 m (Figure 6b) are a feature of the Iceland-Scotland Overflow water (ISOW) that flows mainly through the CGFZ from the eastern into the western Atlantic [e.g., *Dickson and Brown*, 1994; *Saunders*, 1994]. The salinity signal of this water mass is not found in the modeled section investigated here (Figure 6a). The ISOW in the model crosses the MAR farther

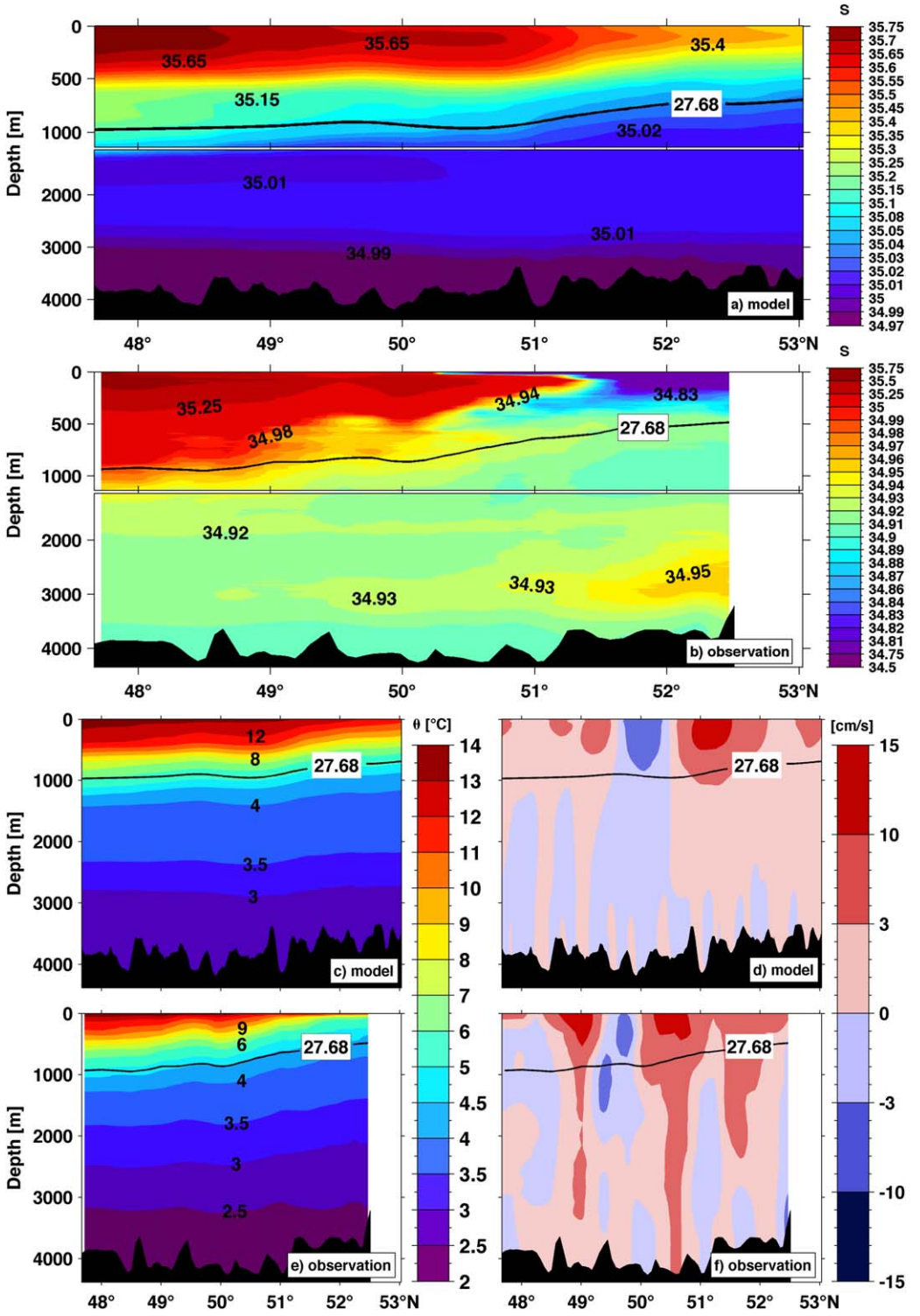

Figure 6. (a and b) Mean salinity, (c and e) potential temperature, and (d and f) velocity section along the PIES array calculated from the last seven model (a, c, and e) years 2002–2008, and (b, d, and f) composite of seven repeat CTD and LADCP sections between 2008 and 2015. Note the different salinity color scales for the model and the observations, which were chosen for visibility reasons. The upper 1000 m are vertically stretched to better display the different salinity distribution. The velocity distributions are defined perpendicular to the PIES array and the velocities toward the northeast are displayed in red. For clarity the observed velocities are treated vertically with a sliding average filter of 600 m length to eliminate the influence of internal waves, which are not present in the model. The modeled sections show the topography from the VIKING20 model, and the observed sections the ETOPO5 [*National Oceanic and Atmospheric Administration*, 1988] topography.

north between 58°N and 60°N and around 30°W (not shown). Part of the difference in the deep ocean is owed to the different vertical resolution of the model (up to several 100 m) and in the observations (1 m).

In the upper 1000 m, salinity and temperature differences almost compensate each other regarding density, so that the depth of the isopycnal $\sigma_\theta = 27.68$ kg m^{-3}, chosen to separate the warm, subtropical NAC water above from the deep water below is nearly the same between observations and model (Figure 6). The isopycnal rises from around 1000 m in the southern part of the section to around 600 m in the model and around 500 m in the observation. The relative steep slope of the isopycnal south of 52°N in the model and south of 51°N in the observation indicate the subpolar front, respectively. In both distributions, a second branch of the subpolar front can be observed, at around 49°30′N in the model and at around 49°N in the observations. In general, modeled and observed velocities are in the same order of magnitude and their vertical and horizontal structures are similar (Figures 6d and 6f). In both cases, the mean velocity distribution is surface-intensified, but mostly reaches down to the bottom, producing horizontally alternating coherent jets over the whole water column. The strongest velocity signal in observations and model is found above the isopycnal $\sigma_\theta = 27.68$ kg m^{-3}, and at the subpolar front, in the model at around 51°20′N, and in the observation further south at around 50°40′N (Figures 6d and 6f).

3.3. Observed and Modeled Transport Time Series at the MAR

At the MAR, a continuous transport time series from 1993 to 2008 provide the means to make the comparison more detailed (Table 1). The mean transports from observations and the model are comparable within the error margins. The mean baroclinic transport in the model referenced to 3400 m depth is 24.6 Sv with a standard deviation of 7.1 Sv. The observed transport of 27.4 Sv with a standard deviation of 4.7 Sv is about 10% higher than the simulated one, but has a lower standard deviation. Compared to observations, the transport in the upper layer is more dominating in the model (70%) than in the observations (60%), caused by a more intensified upper flow. The contribution of the VIKING20 barotropic and ageostrophic components to the mean model transport amounts to about 7%, increasing the mean to 26.4 Sv with a standard deviation of 8.7 Sv. When including the standard deviations of the velocity fluctuations in the reference level [*Rhein et al*., 2011], the observed standard deviation increases to 8.6 Sv, and is very close to the modeled one. The higher absolute transport indicate that also in the real ocean, the barotropic and ageostrophic flow components contribute to the annual means and therefore *Roessler et al*. [2015] slightly underestimate their observed NAC transport. However, this increased transport lies still in the same range of magnitude.

Figures 7 and 8 show the time series of the NAC transports referenced to 3400 m depth from observations and model and also the simulated absolute transports. The annual mean absolute transport is always higher than the baroclinic transport, except for the year 1996. From 1993 to 2004, the observed and simulated baroclinic time series are similar and highly correlated (correlation coefficient of 0.7), while for the years afterwards, the observed transports increase almost linearly until 2008, while the simulated transports reach a minimum of nearly 15 Sv in 2006. In the following time period, the modeled transport rises rapidly and comes close to the observed transport at the end of 2008 (Figure 7). This different behavior of observed and modeled transport will be discussed in section 4.1. The total (baroclinic and barotropic) transport estimates from the PIES instruments alone for the years 2007 and 2008 are close to the observational

Table 1. Mean Absolute and Baroclinic Transport Components From the Model and Observed Mean Transports Across the PIES Array at the MAR and the Subsections Defined by the Geographical Positions of the PIES Instruments[a]

	Modeled Absolute Transport (Sv)		Modeled Baroclinic Transport (Sv)		Observed Transport (Sv)
Subsection of PIES Array	Period: 1960–2008	Period: 1993–2008	Period: 1960–2008	Period: 1993–2008	Period: 1993–2008
Southern	4.5 ± 9.0	3.5 ± 9.1	5.1 ± 8.5	3.9 ± 8.4	8.6 ± 7.7
Central	8.2 ± 10.5	8.0 ± 11.1	8.4 ± 9.4	8.6 ± 10.0	12.2 ± 7.0
Northern	10.0 ±10.5	11.7 ± 12.3	8.6 ± 9.4	9.9 ± 11.0	5.3 ± 3.0
Extended	3.6 ± 6.5	3.1 ± 7.5	2.3 ± 6.2	2.1 ± 7.1	
Entire	26.2 ± 8.8	26.4 ± 8.7	24.5 ±7.1	24.6 ±7.1	27.4 ± 4.7

[a]The transports corresponding standard deviations calculated from the 5 day means are given as well. The extended subsection takes the northward shift of the NAC in the model into account. The sum of the three observed segments (26.1 Sv) does not necessarily agree with the transport of the total array which is calculated independently (27.4 Sv) [*Roessler et al*., 2015].

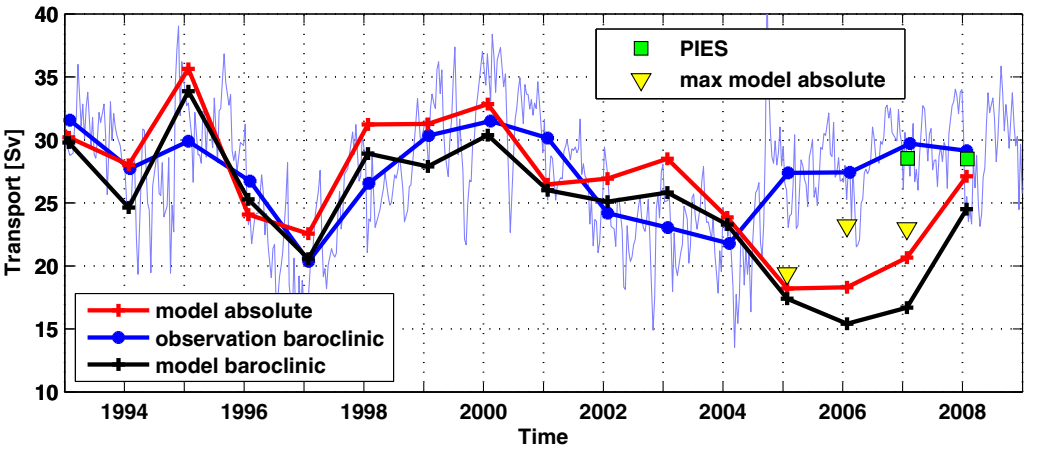

Figure 7. Absolute (red), and baroclinic (black) transport from the VIKING20 model and observed baroclinic (blue) transport time series from 1993 to 2008 at the PIES array along the MAR. The bold lines and markers are annual means and the thin line displays the 10 day values of the altimeter observations. The green squares mark the in situ measurements from the PIES instruments [*Roessler et al*., 2015]. The yellow triangles indicate the maximum transport across the section. The section is extended further north until the maximum transport for that year is found.

transports, as expected since the latter is based on a correlation between the altimetry derived 4 year along-track SSH measurements and PIES derived baroclinic data (Figure 7). The influence of the barotropic fluctuations on the annual means is small due to their short time scales [*Roessler et al*., 2015].

The absolute and baroclinic transports and their variability change only slightly when taking the entire model time period (1960–2008) into account (Table 1 and Figure 8). The longer time series shows that the

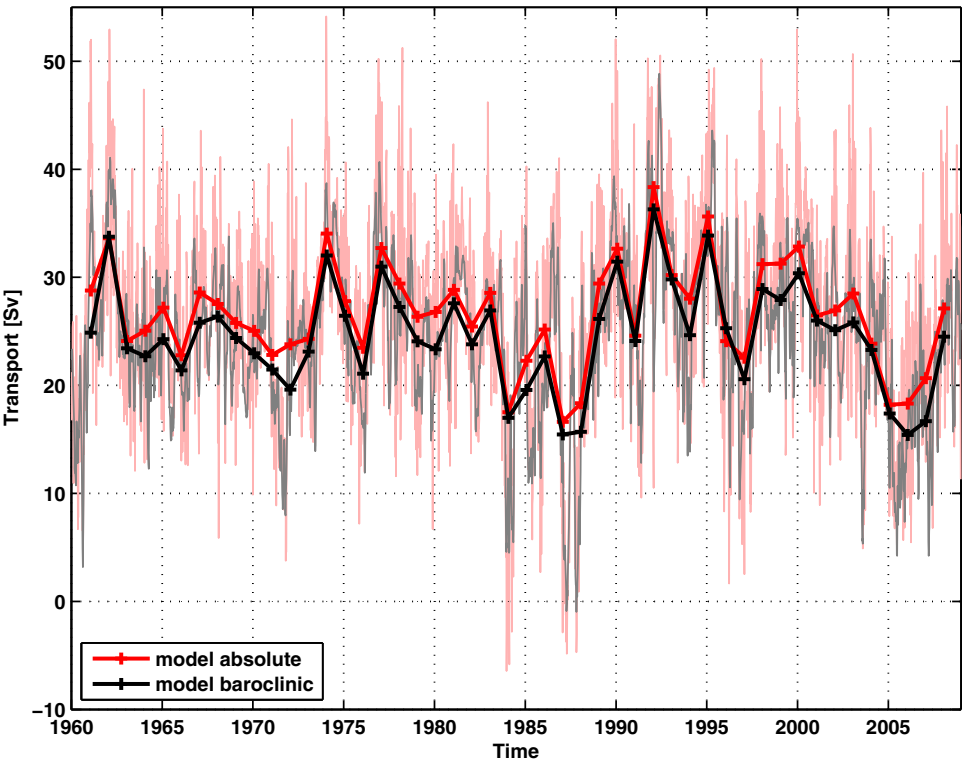

Figure 8. Absolute (red) and baroclinic (black) transport from the VIKING20 model from 1960 to 2008 at the location of the PIES array along the MAR. The bold lines and markers are annual means and the thin lines display the 5 day mean of the model (red and black).

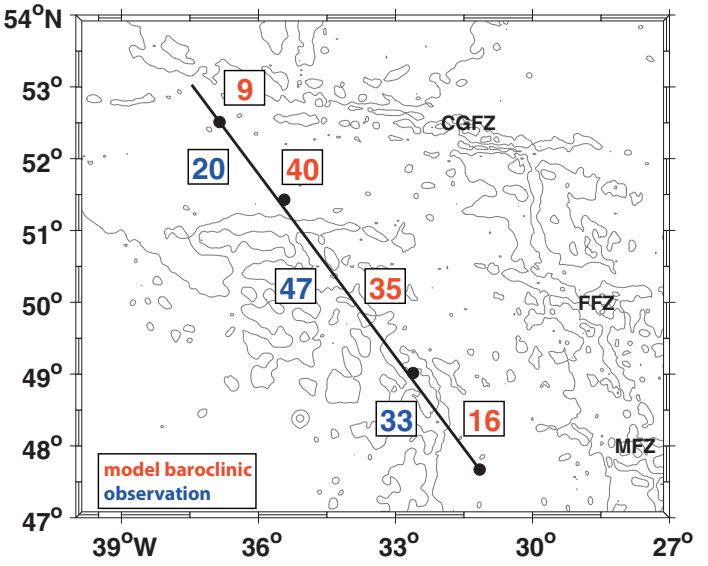

Figure 9. Mean fractions (%) of modeled baroclinic (red) and observed (blue) mean transport relative to 3400dbar calculated from 1993 to 2008. The positions of the PIES are indicated by the black dots [*Roessler et al.*, 2015].

minimum in 2006 is not so uncommon. Similar minima are found in 1972, 1984, and in 1987–1988. The largest annual mean transports occurred in 1992 and in 1995 with values above 34 Sv.

Independent of the time period and transport component, the extended model segment north of 52°30′N contributes about 9–13% of the mean (Figure 9 and Table 1). Overall 57% of the absolute mean transport and 49% of the baroclinic transport are located in the northern and extended segments. The strongest mean transport in the model is found in the northern segment. In the observations, only 20% of the mean transport is found in that segment. The strongest observed mean flow toward the northeast is in the central segment (47%) (Table 1).

As pointed out by *Roessler et al.* [2015], no significant trend in the NAC transport time series was observed. Individual segments, however, had opposing trends, leading to a more focused NAC in the central subsection and decreasing transports in the southern and northern segments (Table 2). This is in contrast to the negative trend in the VIKING20 NAC for the time period 1993 to 2008, caused by the transport decrease between 2005 and 2007 that was not found in the observations. Over the longer 1960–2008 period, no significant trend was found for the absolute nor for the baroclinic NAC transports in the model, but individual segments behave differently (Table 2). While in the observations, the NAC flow gets more focused with time in the central segment, the simulated transports in the central subsection decreased significantly by either around 3 Sv (1960–2008) or 6 Sv (1993–2008). The flow through the extended model segment weakened by about 2 Sv in all time periods. For the years 1960–2008, the weaker flow in the central and the extended subsection is compensated by an intensified flow in the northern subsection, with no significant trends in the southern segment. In 1993–2008, the model exhibits weaker transports in all segments but the southern subsection (Table 2).

Although the seasonal cycles are apparent neither the altimetry transport nor modeled transports show significant seasonal cycles for the time period where observations and model results are available (1993–2008, not shown).

Table 2. Cumulated Trends for the Modeled Absolute, Modeled Baroclinic, and Observed Transport Components for Different Time Periods[a]

	Modeled Absolute Transport Trend (Sv)		Modeled Baroclinic Transport Trend (Sv)		Observed Transport Trend (Sv)
Subsection of PIES Array	Period: 1960–2008	Period: 1993–2008	Period: 1960–2008	Period: 1993–2008	Period: 1993–2008
Southern	0.003 ± 1.2*	2.3 ± 2.1	−0.7 ± 1.1*	1.7 ± 1.9	−1.7 ± 2.5*
Central	−3.4 ± 1.4	−6.0 ± 2.5	−2.7 ± 1.2	−5.7 ± 2.3	3.8 ± 2.2
Northern	5.6 ± 1.4	−2.9 ± 2.8	4.5 ± 1.2	−2.9 ± 2.5	−2.3 ± 0.1
Extended	−2.4 ± 0.9	−2.0 ± 1.7	−1.8 ± 0.8	−2.8 ± 1.6	
Entire	−0.3 ± 1.1*	−8.6 ± 1.9	−0.7 ± 0.9*	−9.7 ± 1.5	−0.8 ± 1.4*

[a]The * marks the nonsignificant trends. The significance is calculated using a two-sided *t* test with a 95% confidence level and the error of the trend is calculated from the 95% confidence bounds for the corresponding time period.

3.4. Transport at the OVIDE Line

The OVIDE data were taken every second year between 2002 and 2010 during the summer months. We compare these data with transports from the model calculated for every second summer (May–July) for the last eight model years (2000–2008). The model simulates well the upper ocean intensified flows and observed and modeled velocity distributions show features with similar horizontal and vertical extensions (Figure 10). However, south of 53°N the modeled velocities are generally weaker than the observed ones. The model shows two alternating strong velocity bands between 56°N and 58°N, also visible in the horizontal distributions at 100 m depth (Figure 3a). This feature is also present in the observations, but weaker and with smaller velocities (Figure 10b).

The strongest velocity band in the observations is found around 54°N, belonging to the western branch of the NAC (WNAC) carrying 12.7 Sv with a standard deviation of 10.5 Sv (Table 3). Starting around the same latitude but extending further north the modeled WNAC is found with a transport of 17.8 Sv with a standard deviation of 5.1 Sv. The broad velocity band between 46°N and 53°30′N in the observation represents the ENAC with a transport of 26.8 Sv and a standard deviation of 7.4 Sv. The modeled ENAC (Figure 10a) starts further north at 47°30′N and carries 7.9 Sv with a standard deviation of 3.6 Sv toward the east (Table 3).

The simulated ENAC and WNAC transport time series are significantly anticorrelated with a correlation coefficient of −0.6 from 1960 to 2008, and the observations in the 2000s also show this anticorrelation pattern (Figure 11). Further north near 60°N such an anticorrelated behavior is found from satellite altimetry data in the poleward flow west and east of the Reykjanes Ridge and in two subbranches east of the Ridge [*Chafik et al.*, 2014].

Over the whole model time period, the ENAC in the model weakens by -2.9 ± 3.0 Sv, while the WNAC transport increases significantly by 6.6 ± 3.4 Sv.

The mean top to bottom transport across the entire OVIDE section from 1960 to 2008 is 13.9 Sv with a standard deviation of 7.8 Sv (Table 3). This is in the same range as the observed mean transport of 14.3 Sv with a standard deviation of 8.9 Sv. In the observations, most of the eastward transport was found in the European basin (following *Mercier et al.* [2015]), encompassing the two NAC branches (23.6 Sv). In the model, the flow through that segment is much weaker (5.7 Sv), and the eastward transports are more focused at the

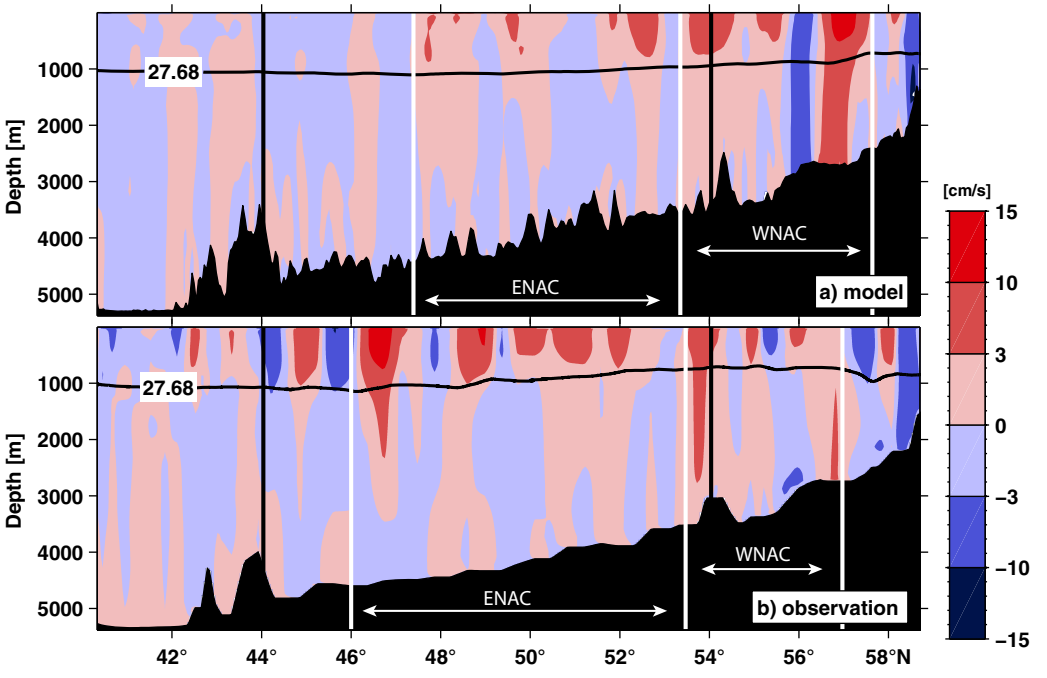

Figure 10. (a) Velocity at the OVIDE line in model and (b) observation [*Mercier et al.*, 2015]. The modeled velocity is the mean from every second year between the years 2000 and 2008. The red velocities are toward the northeast and the blue velocities toward the southwest. The black lines mark the separation in the Iberian, European, and Iceland sections for the transport calculations (Table 3). The white lines separate the flow into the western branch of the NAC (WNAC) and the eastern branch of the NAC (ENAC). The branches are defined by the maximum mean transport toward the northeast.

Table 3. Five Year Mean Transport From Model and Observations Across the OVIDE Line for Different Subsections Along the Line[a]

	Entire Water Column		Subtropical Water (<27.68 kg m^{-3})		Deep Sea (>27.68 kg m^{-3})	
Subsection of OVIDE Line	Model	Observation	Model	Observation	Model	Observation
Iceland basin 54°N to 58.7°N	7.0 ± 4.2	-5.3 ± 9.9	7.9 ± 3.0	-3.3 ± 3.7	-0.8 ± 1.7	-2.0 ± 6.2
European basin 44°N to 54°N	5.7 ± 3.2	23.6 ± 11.4	7.3 ± 2.8	20.1 ± 5.7	-1.5 ± 1.4	3.5 ± 6.6
Iberian basin 40.4°N to 44°N	-2.1 ± 2.2	-3.7 ± 6.6	-1.5 ± 1.3	-2.5 ± 5.0	-0.6 ± 1.2	-1.2 ± 1.7
WNAC	17.8 ± 5.1	12.7 ± 10.5	12.4 ± 2.2	4.3 ± 4.3	5.5 ± 3.2	8.5 ± 6.9
ENAC	7.9 ± 3.6	26.8 ± 7.4	9.2 ± 3.2	23.2 ± 4.3	-1.3 ± 0.9	3.7 ± 4.4
Entire section 40.4°N to 58.7°N	10.5 ± 2.7	14.3 ± 8.9	13.5 ± 1.3	14.3 ± 2.3	-3.0 ± 2.7	-0.03 ± 7.20
WNAC 1960–2008	15.8 ± 7.9		10.5 ± 4.5		5.3 ± 4.2	
ENAC 1960–2008	5.6 ± 8.2		8.2 ± 4.6		-3.2 ± 4.3	
Entire section 1960–2008	13.9 ± 7.8		15.5 ± 3.6		-1.6 ± 5.5	

[a]The top to bottom water column is divided by the $\sigma_\theta = 27.68$ kg m^{-3} isopycnal into subtropical and deep sea water masses. The standard deviations are given. The observed ENAC is defined between 46°N and 53°30′N, where the observed WNAC starts and ends at 57°N. The simulated WNAC starts 0.5° further north at 57°30′N and ends around the same position as the observed one. The simulated ENAC is found between 47°30′N and around 53°30′N (Figure 10). The last three entries show the mean transport and the corresponding standard deviation over the entire model time period for the whole water column and the divided water masses for the WNAC, ENAC and, for the entire section.

Iceland basin (7.0 Sv), while in the observations, the flow in that basin is reversed (−5.3 Sv). The flow in the Iberian Basin is westwards and comparable in model and observations (Table 3).

4. Discussion

4.1. North Atlantic in Model and Observation

In this study, the hydrography, flow field, and transport time series at the western flank of the MAR (the PIES array, *Roessler et al.* [2015]) were investigated using data from a high-resolution hindcast simulation

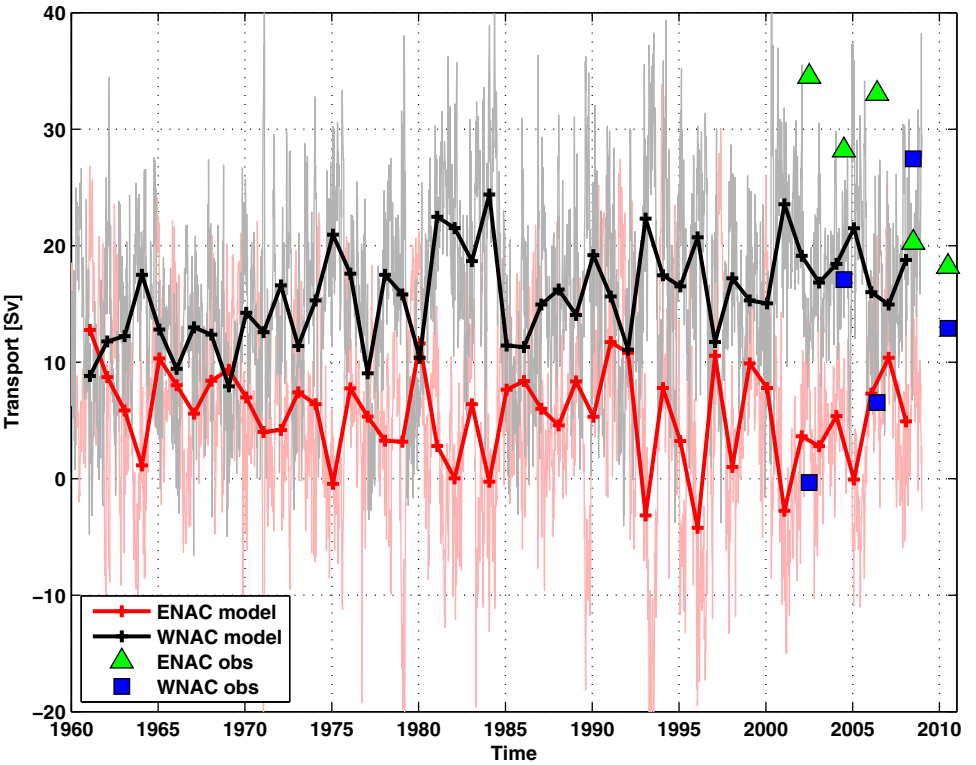

Figure 11. WNAC (black) and ENAC (red) from the VIKING20 model from 1960 to 2008 at the OVIDE line. The bold lines and markers are annual means and the thin lines display the 5 day mean of the model (red and black). The observed WNAC (blue square) and ENAC (green triangle) are marked as well [*Mercier et al.*, 2015].

and observations (PIES, CTD, LADCP, and satellite altimetry measurements). At the PIES array, further upstream in the western Atlantic at 47°N [*Mertens et al*., 2014], and further downstream across the OVIDE line in the eastern Atlantic the mean transports from the model and the observations agree within the standard deviations. However, the model underestimates the observed ENAC mean transport across the OVIDE line. This is not uncommon. The majority of 18 models forced by CORE.v2 data exhibit lower transports than the in situ measurements at the Rapid Climate Change (RAPID) array along 26.5°N [*Danabasoglu et al*., 2014].

In general, the modeled circulation at the MAR is shifted to the north compared to the observations by about half a degree, and in the eastern Atlantic, the more northward located WNAC carries the majority of the transport of the NAC, while in the observations, the ENAC is stronger. One reason for the northward shift could be the more northward penetration of the NAC into the Labrador Sea, thus favoring the more northward pathways for the NAC to the eastern Atlantic. The strength of the SPG of the VIKING20 configuration (about 37 Sv) is comparable with other model configurations forced by CORE.v2 data [*Danabasoglu et al*., 2014] and the observed southward transports at the exit of the Labrador Sea (53°N) of about 37–42 Sv [*Fischer et al*., 2004, 2010; *Xu et al*., 2013].

Despite the different geographical distribution of the flow, the annual mean modeled and observed transports at the MAR for the time period 1993–2004 are significantly correlated (correlation coefficient of 0.7). In the following years (2005–2008), the model shows weaker transports that are not correlated with the observations (Figure 7). During this time period the simulated SSH (not shown) calculated from the area between 15°W–60°W and 48°N–65°N (SPG SSH) diverges from the satellite altimetry SPG SSH [*Danabasoglu et al*., 2016, their Figure 14], which could be one of the reasons for the discrepancies between modeled and observed transports. In models, the SPG SSH is correlated to the intensity of the SPG [*Böning et al*., 2006; *Yeager and Danabasoglu*, 2014; *Danabasoglu et al*., 2016], their correlation coefficient in the VIKING20 model configuration is 0.8. The simulated transport across the MAR section is correlated with the wind stress curl over the SPG region and with the SPG SSH time series.

Furthermore, in the years 2005–2007, the simulated transport at the MAR section is partly shifted toward the north, out of the section we are considering here in comparison to the observations (not shown). Taking this shift into account and calculating the maximum simulated annual transport for 2005–2007 the transport values approach toward the observations (Figure 7), but still show the transport minimum as expected from the simulated SPG SSH.

Although the 2006 transport is the most distinct minimum over the entire time period from 1960 to 2008, similar minima are found in the 1970s and 1980s in the model. The anomalous low transports ($<$20 Sv) affect the whole water column and last over several years, i.e., from 1984 to 1985 and 1987 to 1988, and over 3 years from 2004 to 2006, making it unlikely that a meander or eddy is responsible (Figure 8). However, the transport distributions within the segments show conspicuous reversed flows in some of the subsections. During the 1987 event, the central subsection and the northward extension exhibits a reversed flow, while in 2006, the flow in the northern segment is reversed. The velocity composite for the five weakest transport years (1984, 1987, 1988, 2006, 2007, Figure 12c) reveals that the main pathway across the MAR array is around 1° farther south than in the mean state of the circulation, it shifts from the northern segment to the central part of the section (Figure 12a). Overall, the minimum is found to be affecting the entire NAC and the flow across the MAR section occurs also outside the limit of the section we used for the comparison with the observations. During the minimum periods the NAC exhibits weaker velocities across the entire NA compared to the velocity composite of the five strongest transport years (1962, 1974, 1977, 1992, 1995, Figure 12b). In the eastern Atlantic at the OVIDE line during the minimum transport years the weaker velocity of the WNAC is further influenced by a stronger recirculation than during the maximum transport years. The ENAC in the maximum state shifts slightly toward the west and crosses the OVIDE line in a broader pathway and further south than during the minimum transport years.

During the extreme transport minima (1987, 2006) at the MAR the NAO index is in a neutral state after several years of medium positive NAO (Figure 13). *Lohmann et al*. [2009] found from a model study forced by a persistent positive NAO phase that the subpolar gyre and thus the NAC transport weakens due to advection of warm water from the subtropical gyre.

One has to bear in mind that the observations do not show the transport minimum found in the model between 2004 and 2007, and so it is not surprising that the modeled trend of −8.6 Sv (1993–2008) of

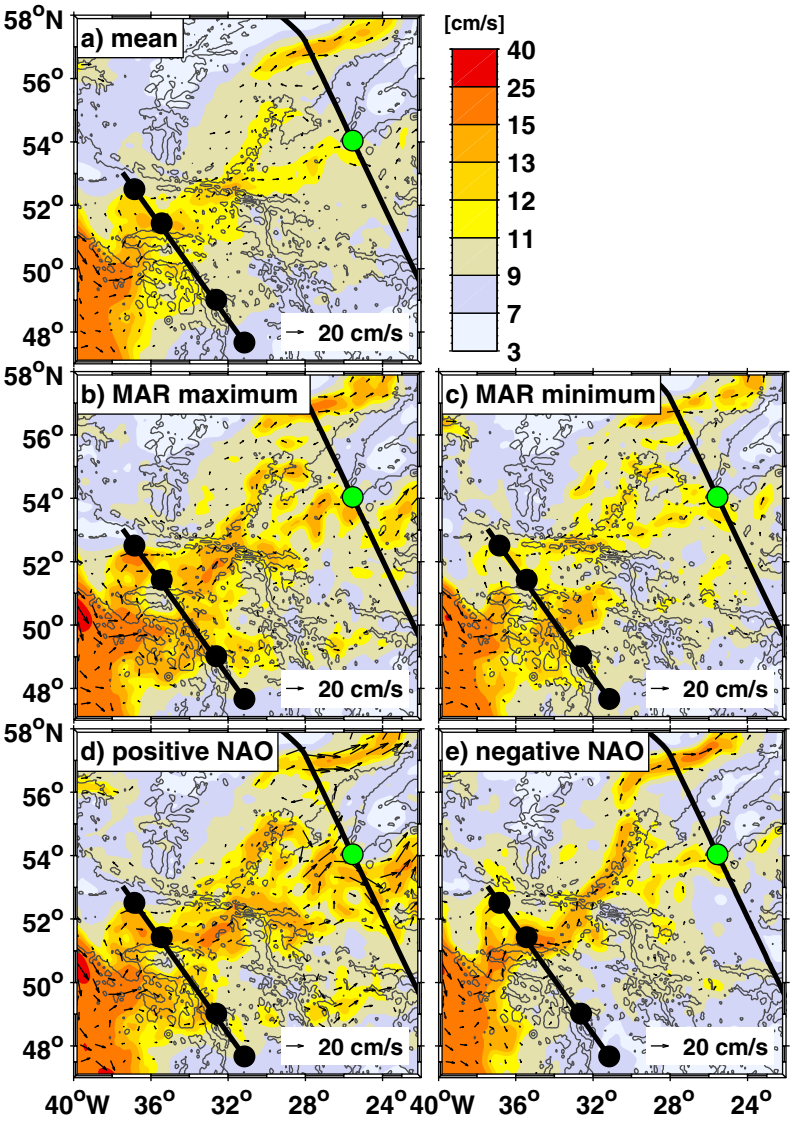

Figure 12. Speed calculated from 1000 m depth to the surface from the model. The velocity time series at each grid point was detrended to eliminate possible long-term trends. (a) The mean velocity for the entire model time period 1960-2008. Composites for the (b) five highest and (c) five lowest transport years at the MAR section. (d) Composites for the five strongest positive NAO phases and (e) the five strongest negative NAO phases. The black lines mark the PIES array and the OVIDE line. The black dots indicate the PIES position and the green dot shows the separation of the OVIDE line into Iceland and European basins after *Mercier et al.* [2015].

the NAC at the MAR is not seen in the observations. The NAC trend over the entire model period from 1960 to 2008 is not significant (−0.3 Sv, Table 2). Further downstream of the NAC, the modeled overall transports at the OVIDE line (not shown) do not show the distinct minima found at the MAR, neither do the individual WNAC or ENAC branch transports (Figure 11). However, during 1960–2008, the modeled WNAC transport strengthened with a positive trend comparable to the increase of 5.6 Sv in the northern segment of the MAR section. Comparable significant positive trends of the AMOC at 26.5°N (1978–1998) and 45°N (1975–1995) are found from the multi model mean over 20 ocean-sea-ice coupled model forced by CORE.v2 [*Danabasoglu et al.*, 2016], the same atmospheric forcing data set used in our model. *Danabasoglu et al.*, [2016] described negative significant trends at both locations from 1996 to 2007 and the rates are nearly double that of the strengthening period. The stronger flow is found to be associated with negative temperature anomalies in the Labrador Sea region, which leads to increased deep water formation, driven by NAO-related surface fluxes [*Yeager and Danabasoglu*, 2014; *Danabasoglu et al.*, 2016].

4.2. Comparison With Other Transport Estimates

There are several programs aiming to measure and understand the NAC, starting with the Florida Current at the RAPID line at 26.5°N, where the mean top to bottom northward transport from up to 300 shipboard sections and 25 years of daily cable observations is around 32 Sv [e.g., *Larsen and Sanford*, 1985; *Cunningham et al*., 2007; *Meinen et al*., 2010; *Johns et al*., 2011; *Meinen and Luther*, 2016]. Recently, *Meinen and Luther* [2016] discussed in detail the evolution of the Gulf Stream transport from the Florida Strait to 42°N, describing the Gulf Stream at different locations as a stream within a channel, a freely meandering jet, and a bounded boundary current, so that we here only give a short summary of observed transport calculations. The transport increases to about 65–94 Sv near Cap Hatteras at 73°W [e.g., *Richardson and Knauss*, 1971; *Halkin and Rossby*, 1985; *Leaman et al*., 1989] and at 70°W to about 95 Sv [*Rossby et al*., 2014]. At 60°W, the Gulfstream is about 5 times higher (150 Sv) than the Florida Current [*Hogg*, 1992]. Further downstream at 50°W, around 80 Sv have been observed [*Clarke et al*., 1980; *Schmitz and McCartney*, 1993], and most of the Gulf Stream turns northward and forms the NAC [*Clarke et al*., 1980; *Rossby*, 1996]. At 42°N, the northward transport including the inshore edge of the Mann Eddy is 146 Sv [*Meinen and Watts*, 2000; *Meinen*, 2001].

Across 47°N, *Mertens et al*. [2014] report from direct measurements that a transport of around 110 Sv flow northwards, with about 45 Sv of subtropical origin (above the $\sigma_\theta = 27.68$ kg m^{-3} isopycnal). Around 35 Sv of the subtropical water recirculates toward the south in the Newfoundland Basin [*Mertens et al*., 2014]. Further downstream across the section at the MAR a mean transport of 18.2 Sv with a standard deviation of 4.7 Sv of subtropical water is found in our model configuration, compatible with the observed transport of about 16 Sv [*Roessler et al*., 2015]. The transport time series is correlated with the transport of the NAC branches WNAC and ENAC across the OVIDE line in the eastern basin. Here the mean transport of subtropical water in the model across both NAC branches of 18.7 Sv with a standard deviation of 4.6 Sv is similar to the mean transport crossing the MAR. Further downstream across 59.5°N east of the crest of the Reykjanes Ridge *Sarafanov et al*. [2012] report from combined measurements between 2002 and 2008 a mean subtropical NAC transport of 15.5 ± 0.8 Sv. They separated the NAC subtropical water mass from the deep ocean with the $\sigma_\theta = 27.55$ kg m^{-3} isopycnal, which lies above the $\sigma_\theta = 27.68$ kg m^{-3} isopycnal that we used in our study at the MAR and the OVIDE line. Using the $\sigma_\theta = 27.55$ kg m^{-3} isopycnal the modeled transport across the MAR reduces to 16.3 Sv with a standard deviation of 4.1 Sv and across both branches of the NAC at the OVIDE line to 16.2 Sv with a standard deviation of 2.9 Sv. The similarity of the mean NAC transports at the MAR and in the eastern Atlantic at the OVIDE line suggest that the subtropical water that crosses 59.5°N entered the eastern basin of the NA via the MAR between 47°N and 53°N. This would mean that in the mean state, all or most of the subtropical water heading toward the Labrador Sea and the Nordic Seas crosses the MAR between 47°N and 53°N and that there is only a weak direct net transport from the subtropical gyre to SPG in the eastern NA. This could be different in a negative NAO state in which the gyres weaken, the polar front moves westward and open an enhanced northward access of the subtropical waters in the eastern boundary current [e.g., *Bersch et al*., 2007]. Over the model time period from 1960 to 2008, the NAO is around two thirds of the time in a positive state and therefore the mean state is biased by the positive NAO pattern. To study the exchange of water between the two different gyres in the eastern NA is beyond the scope of this study and is planned in further modeling and observational studies. For this purpose, moored instruments (current meters, PIES) were successfully deployed along the 47°N latitude in the eastern boundary current and in the eastern basin of the NA in May 2016. From the 16 Sv subtropical NAC, water flowing across the MAR into the eastern NA around 9 Sv cross the Greenland-Scotland Ridge further into the Nordic Seas (B. Hansen, personal communication, 2016), leaving about half of the inflow to remain in the SPG.

4.3. The Influence of the North Atlantic Oscillation on the NAC

Roessler et al. [2015] found that the spectrum of the 21 year observational transport time series at the PIES array along the MAR shows a significant 4–9 year peak, and is significantly cross-correlated with the NAO. The cross correlation is calculated between annual means of the transport time series and the NAO winter index (Figure 13). This approach eliminates partly the effect of meanders and eddies. The monthly influence on the transport is calculated by changing the center of the annual mean transport in each step by 1 month. The probability tests the hypothesis of no correlation by using a *t* statistic with n-2 degrees of freedom, a p-value less than 0.05 indicates a significant correlation. The NAO winter (DJFM) index for observations and model has been computed from the difference of normalized sea level pressures between Ponta

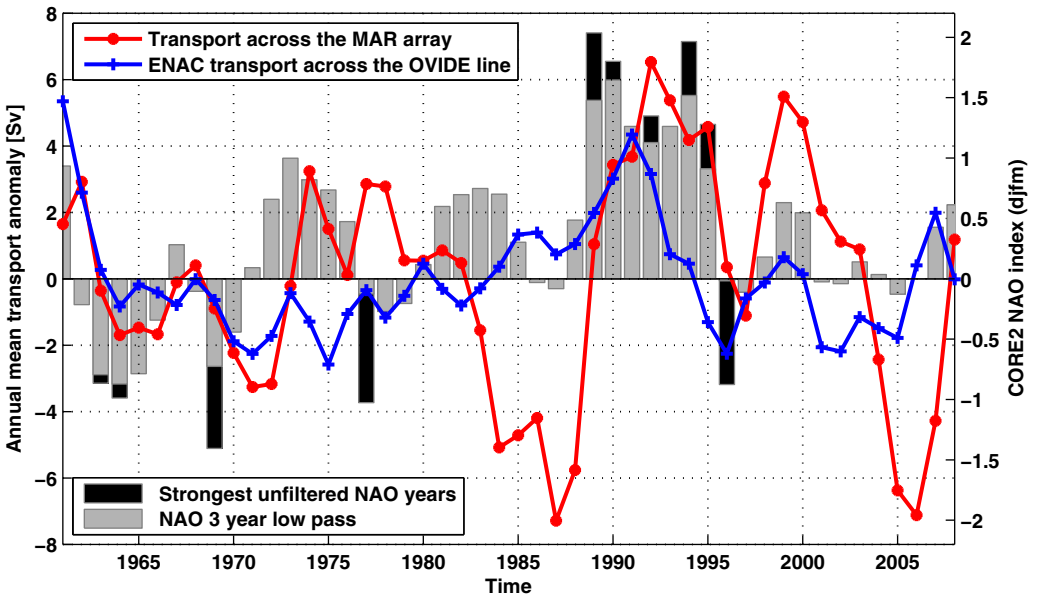

Figure 13. Annual mean transport anomaly across the PIES array at the MAR (red) and the ENAC across the OVIDE line (blue) and winter CORE.v2 NAO (gray). For clarity the time series are treated with a 3 year low pass filter. The black bars mark the five strongest/weakest NAO years, which were used to calculate the composites (Figures 12 and 14) and show the strength of the unfiltered NAO index for that year.

Delgada, Azores and Stykkisholmur/Reykjavik, Iceland [*Hurrell*, 1995], for the modeled NAO the CORE.v2 sea level pressure was used [*Scholz et al*., 2014].

The maximum correlation ($r = 0.49$, $p < 0.01$) between the absolute transport time series at the MAR from 1960 to 2008 in the model and the NAO index is found, when the NAO leads the transport by 7 months. A similar lag is found for the maximum correlation for the baroclinic transport time series, for the model period from 1960 to 2008 the maximum correlation coefficient is 0.54 (with a time lag of 8 months) and from 1993 to 2008, $r = 0.60$ (7 months). These 7–8 months maximum correlation lag time is consistent with the observations from 1993 to 2008 with $r = 0.72$. For the longer time period 1993–2013 *Roessler et al*. [2015] reported that the NAO leads the transport by 6–7 months, with a maximum correlation of $r = 0.5$.

In the eastern basin, the warm subtropical water mass of the ENAC is correlated with the NAO, with a maximum correlation coefficient of $r = 0.37$ when the NAO leads the transport by one month. The short delay time is in agreement with the findings of *Curry and McCartney* [2001], where the NAO index and the ocean gyre index, defined as the baroclinic pressure difference between the subtropical and subpolar gyre centers show similar temporal fluctuations. *Eden and Willebrand* [2001] also reported a fast, intraseasonal response to the NAO, which they found in their model study to be barotropic. An baroclinic oceanic response due to wind stress is described after 6–8 years [*Eden and Willebrand*, 2001]. Hydrographic data of the 1990s show a response in the upper layer of the northern NA within 2 years after the NAO switched from a positive to a negative state [*Bersch*, 2002]. The NAO index leads the multimodel mean AMOC index from 20 global coupled models by 2–4 years [*Danabasoglu et al*., 2016].

Roessler et al. [2015] investigated the composite of the five highest and five lowest NAO index events and found a higher mean transport at the PIES array during the five positive NAO years. This transport increase was mainly found in the southern subsection of the array. One of the highest and three of the lowest NAO event years are found by *Roessler et al*. [2015] in the years after 2008. Here we take the entire model time period into account. The five strongest positive CORE.v2 NAO events are found in the years 1989, 1990, 1992, 1994, and 1995 and the five strongest negative NAO in the years 1963, 1964, 1969, 1977, and 1996 (Figure 13). The five strongest positive NAO events are mainly in the 1990s and the negative NAO events in the 1960s, therefore the difference between the positive and the negative NAO composite might also be biased by other decadal variability. However, similar but weaker results are found if investigating the direct feedback of the NAO by studying transitions from one NAO state to the other (not shown).

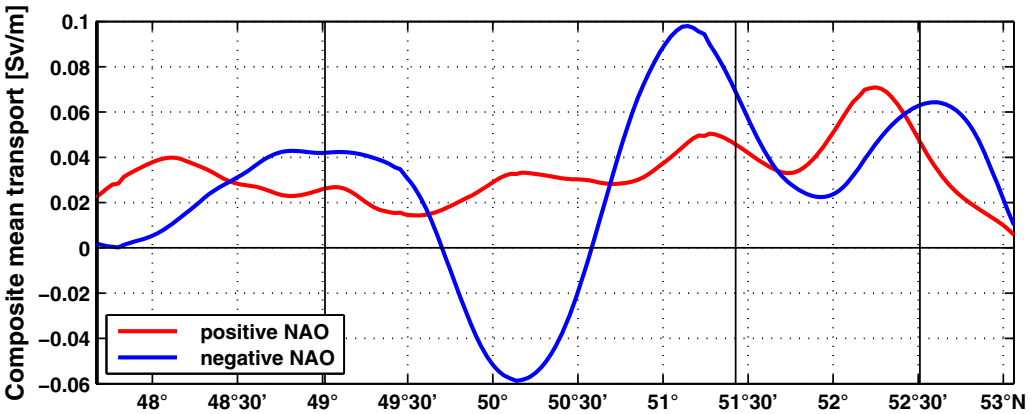

Figure 14. Composites of mean northeastward transports along the PIES section for positive NAO (red) and negative NAO (blue) phases, defined by the five strongest/weakest NAO years. The absolute transport is detrended and calculated from 1000 m depth to the surface, to display the subtropical water mass along the section. The vertical lines mark the PIES positions. The transport is given in Sv/m and the entire section is around 755 km long.

The composites reveal that the mean absolute transport across the PIES array at the MAR during the positive NAO phases (32.9 Sv with a standard deviation of the mean of 1.9 Sv) is significantly higher than during negative NAO phases (26.2 with a standard deviation of the mean of 1.6 Sv). During positive NAO phases significant higher transports cross the entire OVIDE line, except the subsection in the Iceland basin. Here the transport is not correlated with the NAO index. The intensification of the transports is also seen in the western subpolar North Atlantic. During positive NAO years the NWC shifts farther north and is stronger than during negative NAO years, and the recirculation in the Newfoundland basin shows higher velocities as well (not shown). The shift of the NWC is not strong, which is in agreement with the findings of *Stendardo et al*. [2016], who found from observed salinity gradient composites that the position of the NAC off the Grand Banks is slightly shifted westward during positive NAO years. They argue that the impact of the NAO on the ocean is stronger during persistent positive or negative NAO years as shown by *Lohmann et al*. [2009]. During the predominantly negative NAO period in the 1960s the NWC shifted northwestward in the Labrador Basin and an increased Newfoundland basin recirculation was observed by comparing hydrographic data from 1966 with a climatology [*Bersch*, 2002].

The intensification of the NAC and thereby of the subpolar gyre under positive NAO conditions is in agreement with other observations and model results [e.g., *Curry and McCartney*, 2001; *Häkkinen and Rhines*, 2004; *Bersch et al*., 2007; *Häkkinen and Rhines*, 2009**;** *Lohmann et al*., 2009; *Roessler et al*., 2015], but the difference between the two composites of 6.7 Sv for the absolute and 5.1 Sv for the baroclinic transport component in the model is about double the effect seen in the observations at the PIES array (2.9 Sv) [*Roessler et al*., 2015]. This is probably owed to the different time periods chosen for the composites in model and observation. Under positive NAO conditions, the subtropical NAC transport is in the entire section toward the east (Figure 14), with the highest values in the northern part (51°N–52°30′N). During the negative NAO, the transport is much more unevenly distributed, with even westward transports in part of the central segment, and highest transports around 49°N, 51°N, and 52°30′N (Figure 14).

Figure 12 illustrates the different flow fields in the eastern Atlantic, integrated over the upper 1000 m. The more vigorous flow in the positive NAO state is clearly visible. In both cases the main pathway across the MAR is via the CGFZ. This is in agreement with observations which found the northern branch of the NAC passing through this fracture zone [*Rossby*, 1996; *Bower et al*., 2002; *Miller et al*., 2013], although for the period 1993–2013, *Roessler et al*. [2015] reported the dominance of the flow through the FFZ. *Bower and von Appen* [2008] and *Walter and Mertens* [2013] describe single and double branch modes crossing the MAR via the CGFZ, FFZ, and MFZ. East of the MAR the NAC splits into two pathways, the WNAC and the ENAC. During negative NAO phases these pathways are more focused and localized, and the ENAC mean transport is significantly lower by 5.4 Sv than during positive NAO events. This transport change is almost as high as at the MAR, meaning that the main NAO signal is focused on the ENAC. The WNAC transport is not significantly influenced by the NAO and therefore does not change with the NAO phases. The location of the

WNAC and ENAC across the OVIDE line does not change for the different NAO phases. This finding is unexpected and in contrast to other model and observational studies, reporting a zonal shift of the SPG during positive NAO years compared to negative NAO years [e.g., *Curry and McCartney*, 2001; *Chaudhuri et al*., 2011; *Stendardo et al*., 2015].

5. Summary

Circulation and salinity distributions in the NA from 1/20° hindcast model VIKING20 and observations were analyzed. The comparison focused on the hydrography, flow field, and transport time series at the western flank of the MAR and across the OVIDE line in more detail. The transports across the MAR array and the OVIDE line are comparable in model and observations. In general, the circulation at the MAR is shifted to the north in the model compared to the observations by about half a degree, and in the eastern Atlantic, the more northward located WNAC carries the majority of the transport of the NAC, while in the observations, the ENAC is stronger. Neither the observed nor the simulated transport time series across the MAR array show an overall trend. However, due to a not observed minimum in the simulated transport between 2004 and 2007 the simulated transport decreases during the overlapping time period (1993–2008). This minimum is found to be a NA-wide phenomenon in the model, which leads to weaker velocities and different pathways of the NAC. This simulated minimum could be caused by different behavior of the simulated and observed SPG SSH during those years.

The comparison between the model and observations showed that the model simulates the observed transport crossing the MAR and the OVIDE line within the uncertainties, the strength of the velocity field and the NAC. However, it puts the path of the NAC further north, including the NWC and has a preference for the CGFZ and the WNAC in the eastern NA and shows overall higher salinities. Due to the agreement between the observed and simulated transports of the NAC and the correspondence in the flow fields, we used the model to study the atmospheric influence of the NAO on the NAC transports and flow fields. From velocity and transport composites for the five strongest and five lowest NAO years, we found that during positive NAO years higher transport crosses the MAR and the OVIDE line. During this time stronger and more distinct NAC pathways are found.

The overlap between the measurements used here and the VIKING20 model configuration is limited due to the availability of the here used atmospheric forcing (the CORE.v2 data set comprises the years 1948–2009). Further long-term continuous measurements and simulations are needed to study longer-term fluctuations, to improve models by comparing them to observations, and to understand, e.g., the mechanisms behind the here analyzed feedback of the NA circulation to the NAO forcing.

Acknowledgments
We thank Pascale Lherminier, Laboratoire de Physique des Océans, UMR6523, Ifremer, CNRS, IRD, UBO, Plouzané, France for the OVIDE data. We thank two anonymous reviewers for their valuable comments. The altimeter products were produced by Ssalto/Duacs and distributed by Aviso, with support from Cnes (http://www.aviso.altimetry.fr/duacs/). NODC_WOA98 data provided by the NOAA/OAR/ESRL PSD, Boulder, Colorado, USA, from their Web site at http://www.esrl.noaa.gov/psd/. The WOA13 climatology is produced and made freely available by NOAA's National Oceanographic Data Center—Ocean Climate Laboratory (https://www.nodc. noaa.gov/OC5/woa13/). Shipboard data will be submitted to the PANGAEA database and made available to anyone upon request. The model experiment was performed at the North-German Supercomputing Alliance (HLRN). This project was supported by the Deutsche Forschungsgemeinschaft (DFG) through the International Research Training Group "Processes and impacts of climate change in the North Atlantic Ocean and the Canadian Arctic" (IRTG 1904 ArcTrain) (M.R.) and by the German Federal Ministry for Education and Research funded program "RACE" (M.R., C.W.B., A.B.).

References

Barnier, B., et al. (2006), Impact of partial steps and momentum advection schemes in a global ocean circulation model at eddy-permitting resolution, *Ocean Dyn.*, *56*, 543–567, doi:10.1007/s10236-006-0082-1.

Behrens, E. (2013), The oceanic response to Greenland melting: The effect of increasing model resolution, PhD. thesis, Univ. of Kiel, Kiel. [Available at http://macau.uni- kiel.de/receive/dissertation_diss_00013684.]

Bersch, M. (2002), North Atlantic Oscillation–induced changes of the upper layer circulation in the northern North Atlantic Ocean, *J. Geophys. Res.*, *107*(C10), 1–11, doi:10.1029/2001JC000901.

Bersch, M., I. Yashayaev, and K. P. Koltermann (2007), Recent changes of the thermohaline circulation in the subpolar North Atlantic, *Ocean Dyn.*, *57*, 223–235, doi:10.1007/s10236-007-0104-7.

Böning, C. W., M. Scheinert, J. Dengg, A. Biastoch, and A. Funk (2006), Decadal variability of subpolar gyre transport and its reverberation in the North Atlantic overturning, *Geophys. Res. Lett.*, *33*, L21S01, doi:10.1029/2006GL026906.

Böning, C. W., E. Behrens, A. Biastoch, K. Getzlaff, and J. L. Bamber (2016), Emerging impact of Greenland meltwater on deepwater formation in the North Atlantic Ocean, *Nat. Geosci.*, *9*(7), 523–527, doi:10.1038/ngeo2740.

Bower, A. S., and W.-J. von Appen (2008), Interannual variability in the pathways of the North Atlantic Current over the Mid-Atlantic Ridge and the impact of topography, *J. Phys. Oceanogr.*, *38*, 104–120, doi:10.1175/2007JPO3686.1.

Bower, A. S., B. Le Cann, T. Rossby, W. Zenk, J. Gould, K. Speer, P. L. Richardson, M. D. Prater, and H.-M. Zhang (2002), Directly measured mid-depth circulation in the northeastern North Atlantic Ocean, *Nature*, *419*, 603–607, doi:10.1038/nature01078.

Boyer, T., S. Levitus, J. Antonov, R. Locarnini, A. Mishonov, H. Garcia, and S. A. Josey (2007), Changes in freshwater content in the North Atlantic Ocean 1955–2006, *Geophys. Res. Lett.*, *34*, L16603, doi:10.1029/2007GL030126.

Brauch, J. P., and R. Gerdes (2005), Response of the northern North Atlantic and Arctic oceans to a sudden change of the North Atlantic Oscillation, *J. Geophys. Res.*, *110*, C11018, doi:10.1029/2004JC002436.

Chafik, L., T. Rossby, and C. Schrum (2014), On the spatial structure and temporal variability of poleward transport between Scotland and Greenland, *J. Geophys. Res. Ocean*, *119*, 824–841, doi:10.1002/2013JC009287.

Chaplin, G., and D. Watts (1984), Inverted echo sounder development, in *OCEANS 1984*, pp. 249–253, Marine Technology Society, Washington, D. C.

Chaudhuri, A. H., A. Gangopadhyay, and J. J. Bisagni (2011), Contrasting response of the Eastern and Western North Atlantic Circulation to an episodic climate event, *J. Phys. Oceanogr.*, *41*(9), 1630–1638, doi:10.1175/2011JPO4512.1.
Clarke, R. A., H. W. Hill, R. F. Reiniger, and B. A. Warren (1980), Current system South and East of the Grand Banks of Newfoundland, *J. Phys. Oceanogr.*, *10*, 25–65, doi:10.1175/1520-0485(1980)010<0025:CSSAEO>2.0.CO;2.
Cunningham, S. A., et al. (2007), Temporal variability of the Atlantic meridional overturning circulation at 26.5°N, *Science*, *317*(5840), 935–938, doi:10.1126/science.1141304.
Curry, R., and C. Mauritzen (2005), Dilution of the Northern North Atlantic Ocean in recent decades, *Science*, *308*, 1772–1774, doi:10.1126/science.1109477.
Curry, R. G., and M. S. McCartney (2001), Ocean gyre circulation changes associated with the North Atlantic oscillation, *J. Phys. Oceanogr.*, *31*, 3374–3400, doi:10.1175/1520-0485(2001)031<3374:OGCCAW>2.0.CO;2.
Danabasoglu, G., et al. (2014), North Atlantic simulations in Coordinated Ocean-ice Reference Experiments phase II (CORE-II): Part I: Mean states, *Ocean Modell.*, *73*, 76–107, doi:10.1016/j.ocemod.2013.10.005.
Danabasoglu, G., et al. (2016), North Atlantic simulations in Coordinated Ocean-ice Reference Experiments phase II (CORE-II): Part II: Inter-annual to decadal variability, *Ocean Modell.*, *97*, 65–90, doi:10.1016/j.ocemod.2015.11.007.
Daniault, N., et al. (2016), The northern North Atlantic Ocean mean circulation in the early 21st Century, *Prog. Oceanogr.*, *146*, 142–158, doi:10.1016/j.pocean.2016.06.007.
Debreu, L., C. Vouland, and E. Blayo (2008), AGRIF: Adaptive grid refinement in Fortran, *Comput. Geosci.*, *34*(1), 8–13, doi:10.1016/j.cageo.2007.01.009.
Delworth, T. L., and F. Zeng (2016), The impact of the North Atlantic Oscillation on climate through its influence on the Atlantic Meridional Overturning Circulation, *J. Clim.*, *29*(3), 941–962, doi:10.1175/JCLI-D-15-0396.1.
Dickson, R. R., and J. Brown (1994), The production of North Atlantic Deep Water: Sources, rates, and pathways, *J. Geophys. Res.*, *99*(C6), 12,319–12,341, doi:10.1029/94JC00530.
DRAKKAR (2007), Eddy-permitting ocean circulation hindcasts of past decades, *Clivar Exch. No. 42*, vol. *12*, No. 3, pp. 8–10, Int. CLIVAR Proj. Off., Southampton, U. K.
Eden, C., and J. Willebrand (2001), Mechanisms of interannual to decadal variability of the North Atlantic Circulation, *J. Clim.*, *14*, 2266–2280, doi:10.1175/1520-0442(2001)014<2266:MOITDV>2.0.CO;2.
Fichefet, T., and M. A. M. Maqueda (1997), Sensitivity of a global sea ice model to the treatment of ice thermodynamics and dynamics, *J. Geophys. Res.*, *102*(C6), 12,609–12,646, doi:10.1029/97JC00480.
Fischer, J., F. A. Schott, and M. Dengler (2004), Boundary circulation at the exit of the Labrador Sea, *J. Phys. Oceanogr.*, *34*(7), 1548–1570, doi:10.1175/1520-0485(2004)034<1548:BCATEO>2.0.CO;2.
Fischer, J., M. Visbeck, R. Zantopp, and N. Nunes (2010), Interannual to decadal variability of outflow from the Labrador Sea, *Geophys. Res. Lett.*, *37*, L24610, doi:10.1029/2010GL045321.
Fischer, J., et al. (2014), Intra-seasonal variability of the DWBC in the western subpolar North Atlantic, *Prog. Oceanogr.*, *132*, 233–249, doi:10.1016/j.pocean.2014.04.002.
Fratantoni, D. M. (2001), North Atlantic surface circulation during the 1990's observed with satellite-tracked drifters, *J. Geophys. Res.*, *106*(C10), 22,067–22,093, doi:10.1029/2000JC000730.
García-Ibáñez, M. I., P. C. Pardo, L. I. Carracedo, H. Mercier, P. Lherminier, A. F. Ríos, and F. F. Pérez (2015), Structure, transports and transformations of the water masses in the Atlantic Subpolar Gyre, *Prog. Oceanogr.*, *135*, 18–36, doi:10.1016/j.pocean.2015.03.009.
Häkkinen, S., and P. B. Rhines (2004), Decline of subpolar North Atlantic circulation during the 1990s, *Science*, *304*, 555–559, doi:10.1126/science.1094917.
Häkkinen, S., and P. B. Rhines (2009), Shifting surface currents in the northern North Atlantic Ocean, *J. Geophys. Res.*, *114*, C04005, doi:10.1029/2008JC004883.
Halkin, D., and T. Rossby (1985), Structure and transport of the Gulf Stream at 73°W, *J. Phys. Oceanogr.*, *15*, 1439–1452, doi:10.1175/1520-0485(1985)015<1439:TSATOT>2.0.CO;2.
Hauser, T., E. Demirov, J. Zhu, and I. Yashayaev (2015), North Atlantic atmospheric and ocean inter-annual variability over the past fifty years-Dominant patterns and decadal shifts, *Prog. Oceanogr.*, *132*, 197–219, doi:10.1016/j.pocean.2014.10.008.
Hogg, N. G. (1992), On the transport of the Gulf Stream between Cape Hatteras and the Grand Banks, *Deep Sea Res., Part A.*, *39*(7–8), 1231–1246, doi:10.1016/0198-0149(92)90066-3.
Hurrell, J. W. (1995), Decadal trends in the North Atlantic Oscillation: Regional temperatures and precipitation, *Science*, *269*, 676–679, doi:10.1126/science.269.5224.676.
Intergovernmental Panel on Climate Change (IPCC) (2013), Summary for Policymakers, in *Climate Change 2013: The Physical Science Basis. Contribution of Working Group I to the Fifth Assessment Report of the Intergovernmental Panel on Climate Change*, edited by T. F. Stocker, et al., Cambridge Univ. Press, Cambridge, U. K.
Johns, W. E., et al. (2011), Continuous, array-based estimates of Atlantic ocean heat transport at 26.5°N, *J. Clim.*, *24*(10), 2429– 2449, doi:10.1175/2010JCLI3997.1.
Kieke, D., M. Rhein, L. Stramma, W. M. Smethie, J. L. Bullister, and D. A. LeBel (2007), Changes in the pool of Labrador Sea Water in the subpolar North Atlantic, *Geophys. Res. Lett.*, *34*, L06605, doi:10.1029/2006GL028959.
Large, W. G., and S. G. Yeager (2009), The global climatology of an interannually varying air-sea flux data set, *Clim. Dyn.*, *33*, 341–364, doi:10.1007/s00382-008-0441-3.
Larsen, J. C., and T. B. Sanford (1985), Florida Current volume transports from voltage measurements, *Science*, *227*, 302–304.
Lavender, K. L., R. E. Davis, and W. B. Owens (2000), Mid-depth recirculation observed in the interior Labrador and Irminger seas by direct velocity measurements, *Nature*, *407*, 66–69, doi:10.1038/35024048.
Leaman, K. D., E. Johns, and T. Rossby (1989), The average distribution of volume transport and potential vorticity with temperature at three sections accross the Gulf Stream, *J. Phys. Oceanogr.*, *19*, 36–51.
Levitus (1998), World Ocean Database 1998, Introduction, *NOAA Atlas NESDIS 18*, vol. *1*, U.S. Gov. Print. Off., Washington, D. C.
Lherminier, P., H. Mercier, T. Huck, C. Gourcuff, F. F. Perez, P. Morin, A. Sarafanov, and A. Falina (2010), The Atlantic Meridional Overturning Circulation and the subpolar gyre observed at the A25-OVIDE section in June 2002 and 2004, *Deep Sea Res., Part I*, *57*(11), 1374–1391, doi:10.1016/j.dsr.2010.07.009.
Lohmann, K., H. Drange, and M. Bentsen (2009), Response of the North Atlantic subpolar gyre to persistent North Atlantic oscillation like forcing, *Clim. Dyn.*, *32*, 273–285, doi:10.1007/s00382-008-0467-6.
Madec, G. (2008), *NEMO Ocean Engine, Note du Pôle demodélisation*, No. 27, Inst. Pierre-Simon Laplace, Paris, France, ISSN: 1288-1619.

Marzocchi, A., J. J.-M. Hirschi, N. P. Holliday, S. A. Cunningham, A. T. Blaker, and A. C. Coward (2015), The North Atlantic subpolar circulation in an eddy-resolving global ocean model, *J. Mar. Syst.*, *142*, 126–143, doi:10.1016/j.jmarsys.2014.10.007.

Meinen, C. S. (2001), Structure of the North Atlantic current in stream-coordinates and the circulation in the Newfoundland basin, *Deep Sea Res., Part I*, *48*(7), 1553–1580, doi:10.1016/S0967-0637(00)00103-5.

Meinen, C. S., and D. S. Luther (2016), Structure, transport, and vertical coherence of the Gulf Stream from the Straits of Florida to the Southeast Newfoundland Ridge, *Deep Sea Res., Part I*, *112*, 137–154, doi:10.1016/j.dsr.2016.03.002.

Meinen, C. S., and D. R. Watts (2000), Vertical structure and transport on a transect across the North Atlantic Current near 42°N: Time series and mean, *J. Geophys. Res.*, *105*(C9), 21,869–21,891, doi:10.1029/2000JC900097.

Meinen, C. S., M. O. Baringer, and R. F. Garcia (2010), Florida Current transport variability: An analysis of annual and longer-period signals, *Deep Sea Res., Part I*, *57*(7), 835–846, doi:10.1016/j.dsr.2010.04.001.

Mercier, H., et al. (2015), Variability of the meridional overturning circulation at the Greenland-Portugal OVIDE section from 1993 to 2010, *Prog. Oceanogr.*, *132*, 250–261, doi:10.1016/j.pocean.2013.11.001.

Mertens, C., M. Rhein, M. Walter, C. W. Böning, E. Behrens, D. Kieke, R. Steinfeldt, and U. Stöber (2014), Circulation and transports in the Newfoundland Basin, western subpolar North Atlantic, *J. Geophys. Res. Oceans*, *119*, 7772–7793, doi:10.1002/2014JC010019.

Miller, P. I., J. F. Read, and A. C. Dale (2013), Thermal front variability along the North Atlantic Current observed using microwave and infrared satellite data, *Deep Sea Res., Part II*, *98*, 244–256, doi:10.1016/j.dsr2.2013.08.014.

National Oceanic and Atmospheric Administration (1988), Data announcemant 88-MGG-02: Digital relief of the surface of the Earth, technical report, Natl. Geophys. Data Cent., Boulder, Colo.

Pérez-Brunius, P., T. Rossby, and D. R. Watts (2004), Absolute transports of mass and temperature for the North Atlantic Current-Subpolar Front System, *J. Phys. Oceanogr.*, *34*(8), 1870–1883, doi:10.1175/1520-0485(2004)034<1870:ATOMAT>2.0.CO;2.

Rhein, M., D. Kieke, S. Hüttl-Kabus, A. Roessler, C. Mertens, R. Meissner, B. Klein, C. W. Böning, and I. Yashayaev (2011), Deep water formation, the subpolar gyre, and the meridional overturning circulation in the subpolar North Atlantic, *Deep Sea Res., Part II*, *58*, 1819–1832, doi:10.1016/j.dsr2.2010.10.061.

Richardson, P. L., and J. A. Knauss (1971), Gulf stream and Western boundary undercurrent observations at Cape Hatteras, *Deep Sea Res. Oceanogr. Abstr.*, *18*(11), 1089–1109, doi:10.1016/0011-7471(71)90095-7.

Roessler, A., M. Rhein, D. Kieke, and C. Mertens (2015), Long-term observations of North Atlantic Current transport at the gateway between western and eastern Atlantic, *J. Geophys. Res. Oceans*, *120*, 4003–4027, doi:10.1002/2014JC010662.

Rossby, T. (1996), The North Atlantic Current and surrounding waters: At the crossroads, *Rev. Geophys.*, *34*(4), 463–481, doi:10.1029/96RG02214.

Rossby, T., C. N. Flagg, K. Donohue, A. Sanchez-Franks, and J. Lillibridge (2014), On the long-term stability of Gulf Stream transport based on 20 years of direct measurements, *Geophys. Res. Lett.*, *41*, 114–120, doi:10.1002/2013GL058636.

Sarafanov, A., A. Falina, H. Mercier, A. Sokov, P. Lherminier, C. Gourcuff, S. Gladyshev, F. Gaillard, and N. Daniault (2012), Mean full-depth summer circulation and transports at the northern periphery of the Atlantic Ocean in the 2000s, *J. Geophys. Res.*, *117*, C01014, doi:10.1029/2011JC007572.

Saunders, P. M. (1994), The flux of overflow water through the Charlie-Gibbs Fracture Zone, *J. Geophys. Res.*, *99*(C6), 12,343–12,355, doi:10.1029/94JC00527.

Schmitz, W. J., and M. S. McCartney (1993), On the North Atlantic Circulation, *Rev. Geophys.*, *31*(1), 29–49, doi:10.1029/92RG02583.

Scholz, P., D. Kieke, G. Lohmann, M. Ionita, and M. Rhein (2014), Evaluation of Labrador Sea Water formation in a global Finite-Element Sea-Ice Ocean Model setup, based on a comparison with observational data, *J. Geophys. Res. Oceans*, *119*, 1644–1667, doi:10.1002/2013JC009232.

Smith, R. D., M. E. Maltrud, F. O. Bryan, and M. W. Hecht (2000), Numerical Simulation of the North Atlantic Ocean at 1/10°, *J. Phys. Oceanogr.*, *30*, 1532–1561, doi:10.1175/1520-0485(2000)030<1532:NSOTNA>2.0.CO;2.

Stendardo, I., D. Kieke, M. Rhein, N. Gruber, and R. Steinfeldt (2015), Interannual to decadal oxygen variability in the mid-depth water masses of the eastern North Atlantic, *Deep Sea Res., Part I*, *95*, 85–98, doi:10.1016/j.dsr.2014.10.009.

Stendardo, I., M. Rhein, and R. Hollmann (2016), A high resolution salinity time series 1993-2012 in the North Atlantic from Argo and Altimeter data, *J. Geophys. Res. Oceans*, *121*, 2523–2551, doi:10.1002/2015JC011439.

Stramma, L., D. Kieke, M. Rhein, F. Schott, I. Yashayaev, and K. P. Koltermann (2004), Deep water changes at the western boundary of the subpolar North Atlantic during 1996 to 2001, *Deep Sea Res., Part I*, *51*(8), 1033–1056, doi:10.1016/j.dsr.2004.04.001.

Talley, L. D., and M. S. McCartney (1982), Distribution and circulation of Labrador Sea Water, *J. Phys. Oceanogr.*, *12*(11), 1189–1205, doi:10.1175/1520-0485(1982)012<1189:DACOLS>2.0.CO;2.

U.S. Department of Commerce (2001), *Global Gridded 2-minute Database, Natl.* Oceanic and Atmos. Admin. Natl. Geophys. Data Cent. (NGDC), Boulder, Colo. [Available at http://www.ngdc.noaa.gov/mgg/global/etopo2.html.]

Walter, M., and C. Mertens (2013), Mid-depth mixing linked to North Atlantic Current variability, *Geophys. Res. Lett.*, *40*, 4869–4875, doi:10.1002/grl.50936.

Watts, D. R., and H. T. Rossby (1977), Measuring dynamic heights with inverted echo sounders: Results from MODE, *J. Phys. Oceanogr.*, *7*(3), 345–358, doi:10.1175/1520-0485(1977)007<0345:MDHWIE>2.0.CO;2.

Xu, X., H. E. Hurlburt, W. J. Schmitz, R. Zantopp, J. Fischer, and P. J. Hogan (2013), On the currents and transports connected with the Atlantic meridional overturning circulation in the subpolar North Atlantic, *J. Geophys. Res. Oceans*, *118*, 502–516, doi:10.1002/jgrc.20065.

Yeager, S., and G. Danabasoglu (2014), The origins of late-twentieth-century variations in the large-scale North Atlantic Circulation, *J. Clim.*, *27*(9), 3222–3247, doi:10.1175/JCLI-D-13-00125.1.

Zweng, M. M., et al. (2013), World Ocean Atlas 2013, Volume 2: Salinity, S. Levitus, Ed., A. Mishonov, Technical Ed., *NOAA Atlas NESDIS 74*, 39 pp., Silver Spring, Md.